NOISE SUPPRESSION FOR SPECTRAL CT IMAGING

A Thesis
Presented to
The Academic Faculty

by

Joseph M Harms

In Partial Fulfillment
of the Requirements for the Degree
Masters of Science in Medical Physics in the
School of Mechanical Engineering

Georgia Institute of Technology
December 2015

NOISE SUPPRESSION FOR SPECTRAL CT IMAGING

Approved by:

Dr. Lei Zhu, Advisor
School of Mechanical Engineering
Georgia Institute of Technology

Dr. C-K Chris Wang
School of Mechanical Engineering
Georgia Institute of Technology

Dr. Justin Roper
Department of Radiation Oncology
Emory University School of Medicine

Dr. Anna Erickson
School of Mechanical Engineering
Georgia Institute of Technology

Date Approved: December 1, 2015

ACKNOWLEDGEMENTS

I would like to thank my advisor, Dr. Lei Zhu, for contributing copious amounts of time and resources to mentoring and guiding me both as a student and as a researcher. Additionally, I would like to thank my committee members, Dr. Anna Erickson, Dr. Justin Roper, and Dr. C-K Chris Wang for additional advice and guidance throughout my research and graduate studies at Georgia Tech.

I would like to thank my labmates Michael Petrongolo and Tonghe Wang for excellent guidance and constructive conversation which helped to form the basis of my thesis work.

Additionally I would like to thank my parents, Mark and Julie, for their unconditional support throughout all of my education.

TABLE OF CONTENTS (NEED TO FIX)

LIST OF TABLES

LIST OF FIGURES

LIST OF ABBREVIATIONS

CNR	contrast-to-noise ratio
CT	computed tomography
DECT	dual-energy computed tomography
diag	diagonal matrix
FBP	filtered backprojection
HU	Hounsfield unit
kVp	kilovoltage peak
LDPE	low-density polyethylene
NPS	noise power spectrum
PMP	polymethylpentene
PWLS-EPR	penalized weighted least-square with edge-preserving regularization
PWLS-SBR	penalized weighted least-square with similarity based regularization
RMSE	root-mean-square error
ROI	region of interest
SNR	signal-to-noise ratio
STD	standard deviation
var	variance

Chapter 1 - Introduction

Dual-energy CT (DECT) was first introduced in 1976 by Alvarez and Macovski[1]. The main advantage offered by DECT comes from the ability to distinguish materials within an image through a process known as material decomposition. Material decomposition in diagnostic imaging is based on the fact that there are two primary mechanisms of photon interaction with matter in the diagnostic energy range, photoelectric effect and Compton scattering. The object contained within the image can ben be broken down into materials based on its method of interaction with photons.

Material decomposition has created wide clinical applications for dual-energy imaging, including iodine quantification[2, 3], kidney stone characterization[4-6], virtual monochromatic imaging[7-9], lung perfusion/ventilation studies[10], virtual non-enhanced imaging[11-13], aortic pathologies[14], diagnosis of pulmonary emboli[15], and neurological and cerebral vascular imaging[16, 17].

Although DECT has found applications in diagnostics, it is fundamentally limited by significant noise amplification, leading to degradation of the signal-to-noise ratio[18-21]. Noise suppression methods, both general to all of image processing and specific to DECT, have been explored. Many of the existing methods achieve acceptable noise suppression, however they typically lead to decreases in accuracy, poor image quality, or loss of spatial resolution. The intention of this research is to develop a noise suppression method which not only reduces noise, but preserves image quality and spatial resolution. We will present a background discussing noise characteristics in CT imaging and specific

to DECT, current noise suppression methods, and then present the formulation of our noise suppression algorithm accompanied by phantom and patient results.

Chapter 2 - Background

2.1 Concept of Basis Material Decomposition

Material decomposition is based on the fact that in the diagnostic energy range there are two primary mechanisms of photon interaction with matter, i.e., photoelectric absorption and Compton scattering, and the linear attenuation coefficient is a summation of the probabilities of these interactions. These mechanisms of interaction are governed by known functions which are dependent on both the material's atomic number and the photon's energy. Fig. 1 shows the probability of each interaction, along with coherent scattering (which can be ignored in the diagnostic energy range), for water and iodine. Fig. 2 shows the total mass attenuation coefficient (linear attenuation coefficient divided by material density) for various materials. In material decomposition, this information is used to determine the material composition based on attenuation properties at the two different energy-levels. The material images produced by this process represent the relative fraction of two different materials, typically a bone-like (highly attenuating) and tissue-like (moderately attenuating) material. This material differentiation is the main advantage of DECT.

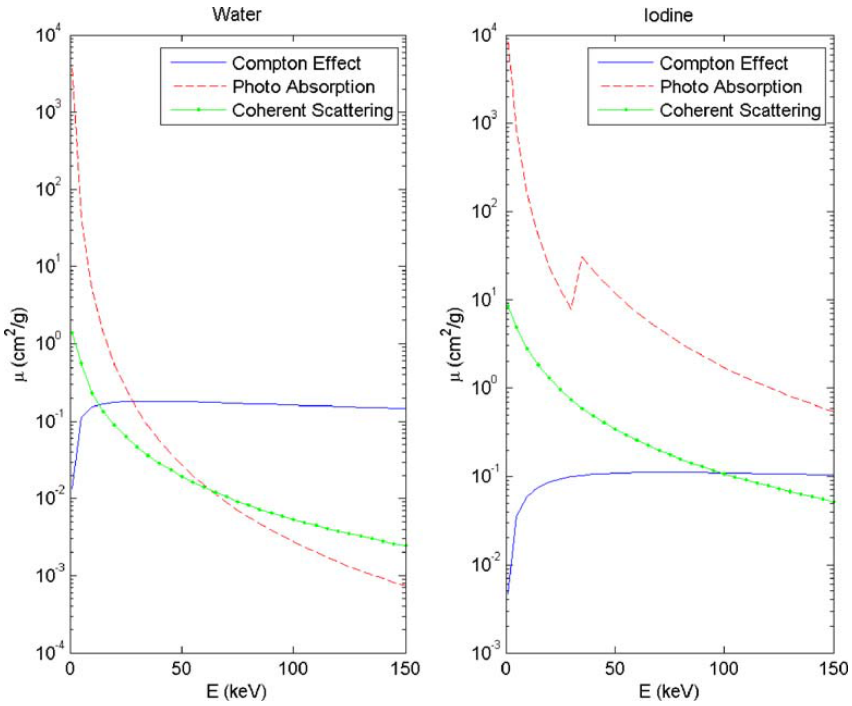

Figure 1. Mass attenuation coefficient for each interaction mechanism (i.e. Compton effect, photoelectric absorption, and coherent scattering) for water and iodine[22].

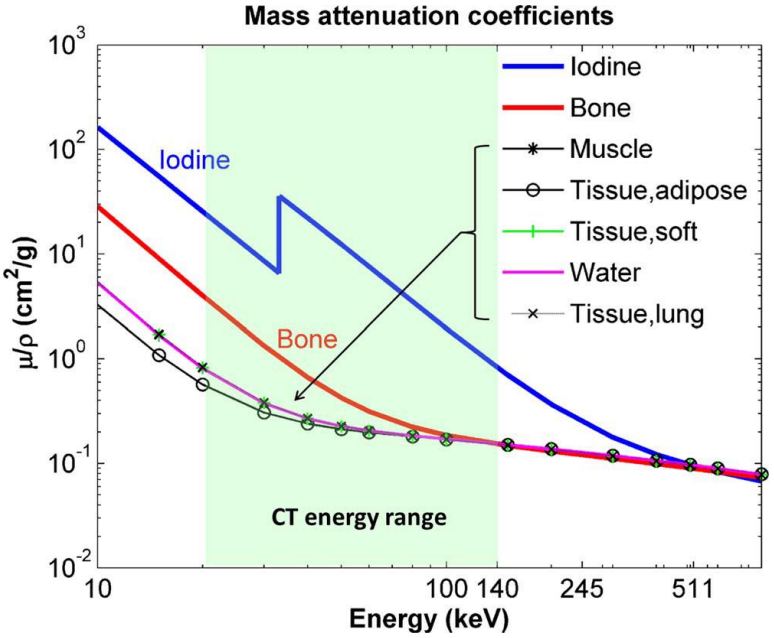

Figure 2. Mass attenuation coefficient for various materials in the diagnostic energy range[23].

2.2 Applications of DECT

Material decomposition is commonly used in determination of the composition of kidney stones. Kidney stones can be composed of different materials, namely uric-aced based or non-uric based, and these compositions can provide information on the underlying cause of the kidney stone. With conventional CT, the difference between attenuation coefficient between uric acid-based stones and non-uric acid-based stones is too small to determine the composition of the stone. However, with dual-energy CT this becomes possible based on the varying attenuation properties of the different stones. CT values in Hounsfield units (HU)for the different stones at low and high energies are plotted in Fig. 3. Hounsfield units are the common clinical unit for CT value, and are formulated as:

$$HU = \frac{(\mu_x - \mu_w)}{\mu_w} \times 1000 \quad (1)$$

where μ_x is the linear attenuation coefficient of material *x,* and μ_w is the linear attenuation coefficient of water. If the stone in question falls below the midline separating a "pure" uric acid stone and a "pure" non-uric acid stone, as the hollow circle does, it is labelled as an uric acid stone. Examples of kidney stone composition differentiation are shown in Figs. 4 and 5.

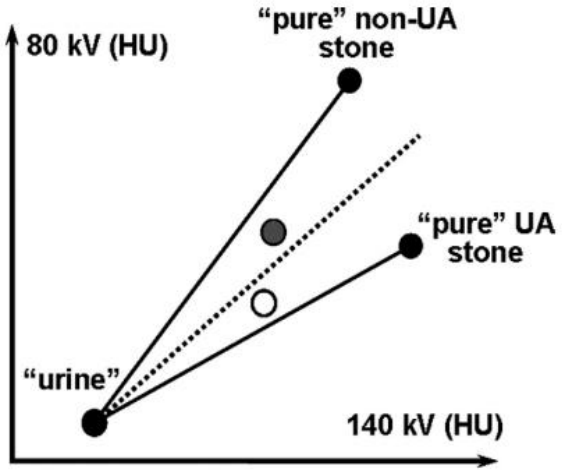

Figure 3. CT value of uric acid stones and non-uric acid kidney stones[4].

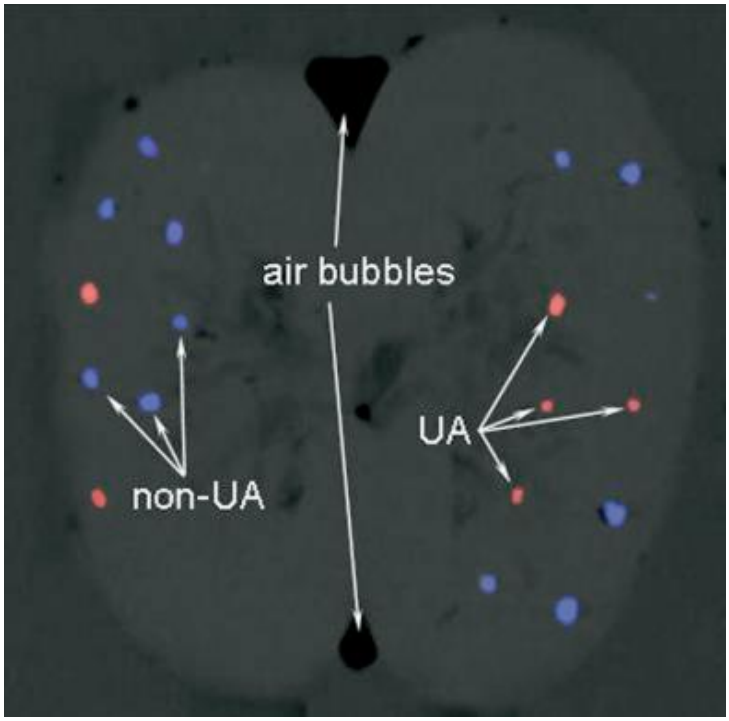

Figure 4. Example of several kidney stones of various chemical compositions inserted into porcine kidneys. Red indicates the presence of uric acid (UA) while blue indicates a lack of uric acid (non-UA)[4].

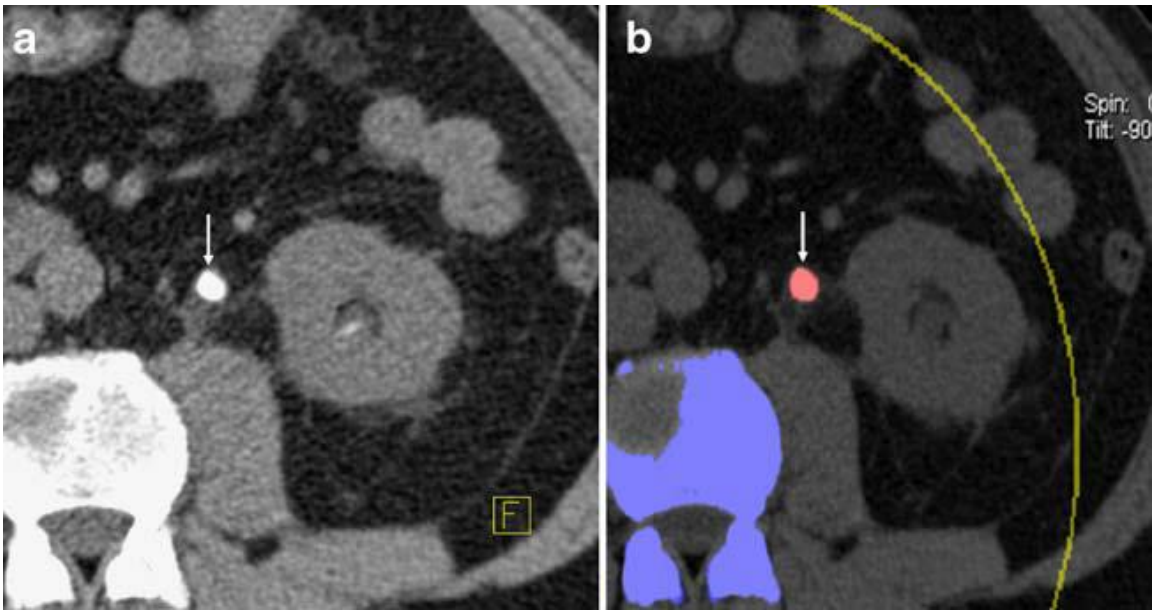

Figure 5. Clinical application of kidney stone characterization. In the CT image (left), the stone is indistinguishable from bone, while the material image (right) superimposed on the CT image shows that the bone and the stone are different materials[24].

Dual-energy CT can also be used to make virtual monochromatic images which are free from beam-hardening, as shown in Fig. 6. These are created much in the same manner as electron density images (section 3.5), with attenuation coefficient of each material (at the energy of the monochromatic image) replacing the electron density shown in Eqn. (18)[9].

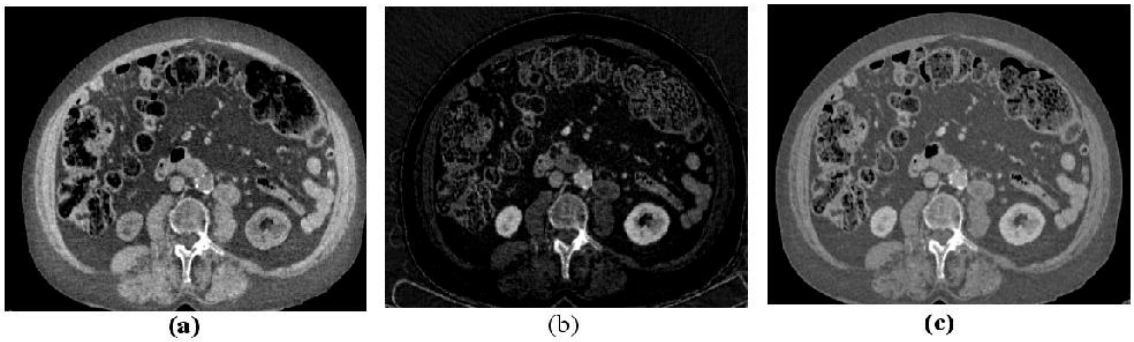

Figure 6. (a) water density image, (b) iodine density image, and (c) monochromatic image at 75 keV[9].

Additionally, DECT has found implications in perfusion studies of the lungs[10]. In this case, the patient's blood vessels are injected with iodine. In material decomposition, an iodine map is created then superimposed on the CT image for localization. These studies are used in diagnosis of pulmonary emboli. The images are compared to SPECT/CT studies, and are shown in Fig. 7. DECT yields a great clinical advantage in this scenario because of the superior spatial resolution of CT compared to SPECT.

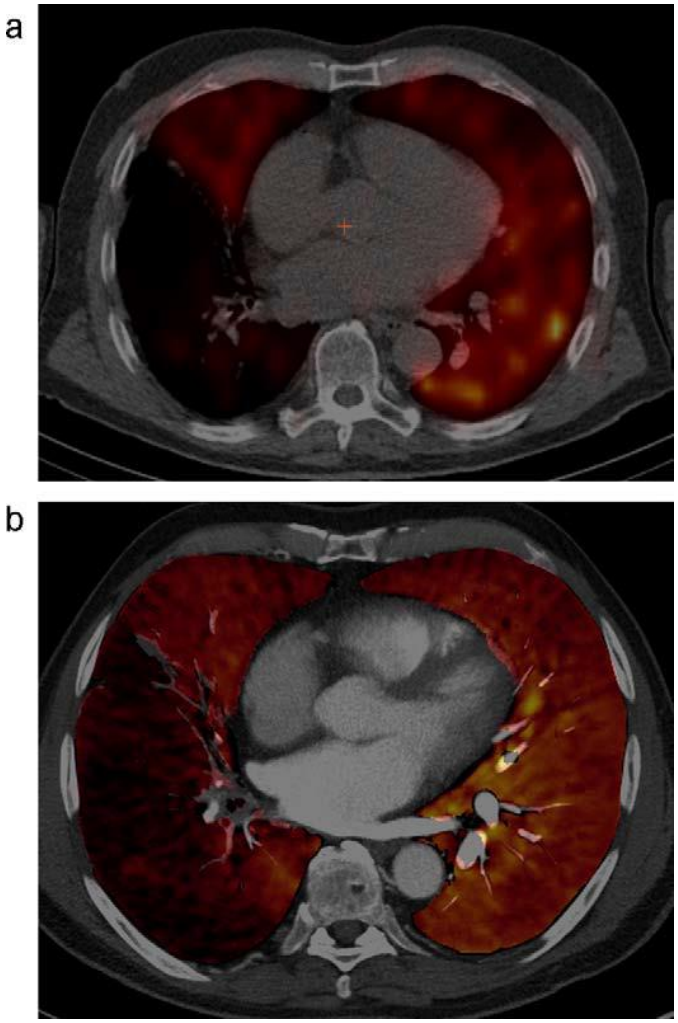

Figure 7. SPECT/CT fused perfusion image (a) and DECT fused image/iodine map of a patient with perfusion defect in the right lower lobe[10].

2.3 Dual-energy CT Scanners

Although DECT was first proposed in 1976, it was not widely implemented until recent years due to limits in CT scanner technology. Three scanner designs are currently being produced for clinical use.

The first type of scanner, the Siemens SOMATOM Definition Flash, is a 64-slice (or 128-slice) dual-source CT which consists of two x-ray tubes, offset by 90 degrees, operated simultaneously at two different tube voltages, and two detectors. As image noise is dependent on the number of photons which reach each detector pixel, and low-energy photons are preferentially absorbed in the object, the low-energy image will have higher noise levels than the high-energy image. The SOMATOM Definition accounts for this phenomena by adjusting the current in each tube so that the lower energy beam contains more photons, allowing for matching noise levels on each CT image. The main feature of this system is speed, having a rotation time of 0.33s compared with 0.5s or 1.0s on other 64-slice scanners[25]. This faster rotation time and increased temporal resolution make the SOMATOM ideal for cardiac imaging in addition to other dual-energy applications.

However, the dual-source design has a few drawbacks. Due to limited space in the gantry, one detector has to be smaller than the other, producing two different field sizes, as seen in Figs. 8 and 9. The small field-of-view makes applications through thicker parts of the patient, such as the pelvis, limited, especially for larger patients. This has partially been accounted for by using the information from the larger field to extrapolate rays to the smaller field[25], however this is not a perfect solution. Additionally the dual-source method induces a large amount of cross-scatter. Since both beams are on at the same time,

photons from beam A can be scattered into detector B, and vice versa. The effect decreases the contrast-to-noise ratio (CNR), and can lead to an offset ranging from 35 to 188 HU[26].

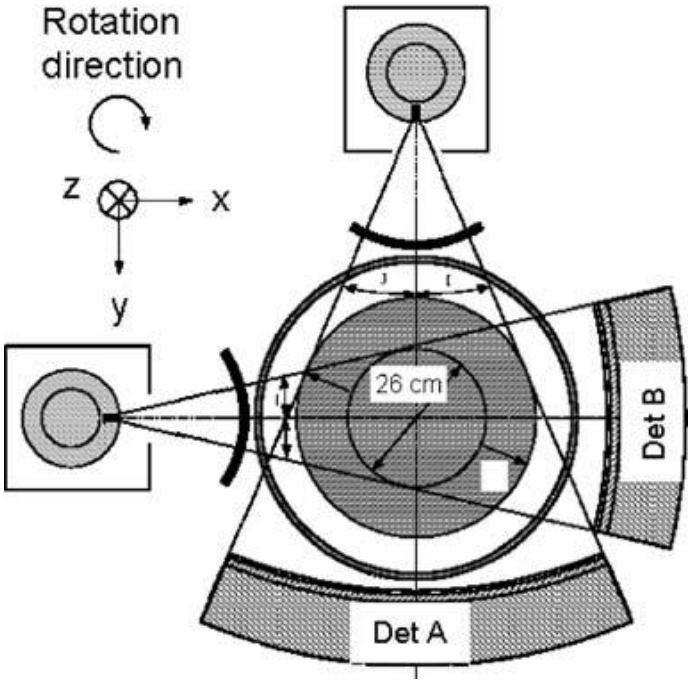

Figure 8. Cross-section of Siemens SOMATOM Definition Flash dual-source CT scanner. ***** make [28] in plain text version

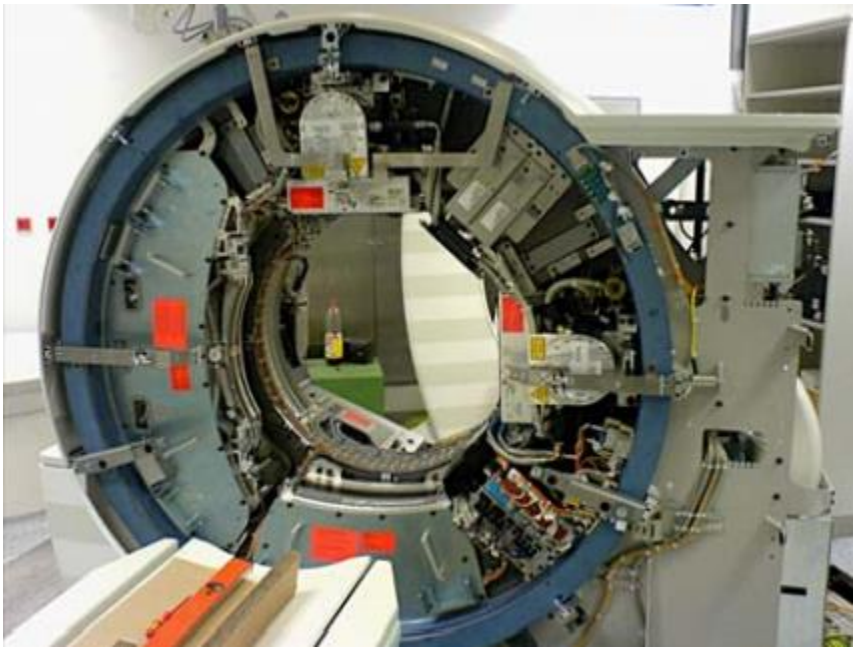

Figure 9. Siemens SOMATOM Definition Flash dual-source CT scanner with gantry housing removed.

GE's clinical dual-energy CT scanner, the Revolution HD, uses only one x-ray source, and changes the tube voltage in between projections, as depicted in Fig. 10. By alternating rapidly from 80 kVp to 140 kVp, this machine acquires the low and high energy projections with much better temporal resolution than the dual-source machines, reducing the time between projections from 75 ms to 0.3-0.5 ms[27]. Additionally, projections can be more easily angularly matched because of the smaller separation between them. This matching makes projection-domain decomposition more easily implementable than on dual-source CT scanners. This also allows for full field-of-view for both energies and eliminates the cross-scatter problems that arise from the dual-source scanner. However, while the Revolution HD alleviates some of the problems of the SOMATOM scanners, it induces some of its own issues. The ideal waveform for the energy switching would be a

square wave, with the tube current jumping exactly from 80 kVp to 140 kVp and vice versa. In reality, the voltage follows a more sinusoidal wave, with effective tube energies climbing and dropping imperfectly[28]. This leads to larger amounts of spectral overlap than are present on the dual-source CT, which can lead to higher levels of noise amplification in material decomposition[18]. Additionally, the tube current cannot be modulated in between projections, leading to noisier low-energy images.

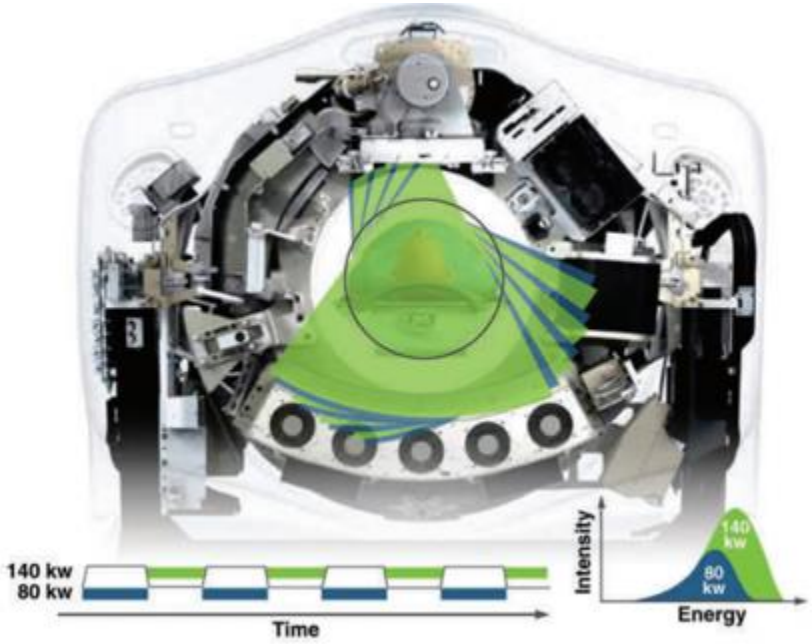

Figure 10. Fast-kVp switching CT scanner[29].

The Phillips solution to the problem of DECT acquisition is a dual-layer "sandwich" detector, the IQon spectral CT scanner. This detector consists of two detecting layers stacked on top of each other, with the top layer, an yttrium-based scintillator, designed to be sensitive to low-energy photons and the bottom layer, a GOS scintillator,

designed to be sensitive to high-energy photons. There are a few advantages to this approach. First, it has zero spectral overlap; acquisition is of only one spectrum with the low energy photons being absorbed in the first detector and the high energy photons being absorbed in the second detector. Additionally, it allows for perfect angular matching of projections since the high and low-energy detectors are in the exact same positions[30]. However, this also method also induces a noise problem because of each detector effectively sees half of the beam, and fewer photons are detected in each detector.

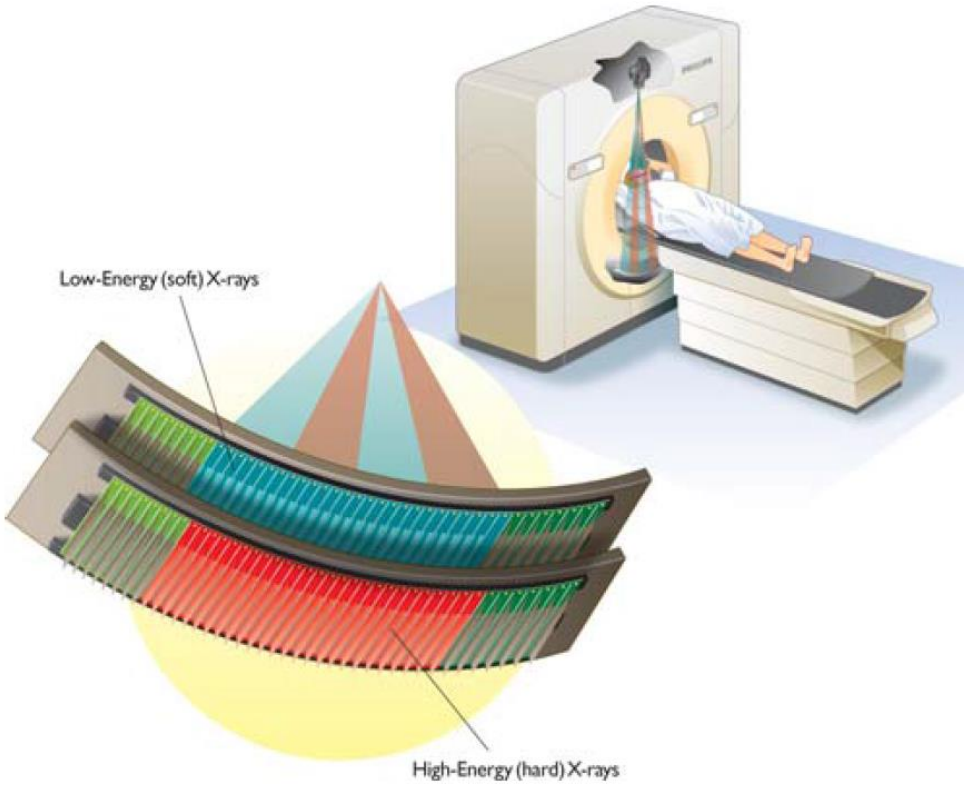

Figure 11. Phillips dual-layer CT detector design, with the scanner shown in the background.

All of these clinical solutions offer a means to wider clinical implementation of dual-energy CT. Although they all bring different advantages and disadvantages, they all introduce a problem relating to noise. When coupling this additional noise with the significant noise amplification inherent of the material decomposition process, it becomes apparent that noise reduction methods are needed. It is this need for noise reduction in DECT that has primarily motivated this research. While hardware modifications could help with noise reduction, we choose to investigate a software-based approach that could be implemented on all three of the scanners.

2.4 Formulation of Basis Material Decomposition

Decomposition can be carried out in either the projection domain[1, 21, 31-33] or the image domain[19, 34, 35]. In projection domain decomposition, the measured projections are converted into line integrals of the basis materials using a non-linear model[1, 34, 36]. Reconstruction of basis material images is then carried out using these line integrals. Decomposition in the projection domain has the advantage of being able to correct for beam-hardening artifacts[1, 33]. However, this requires raw projection data which may not be readily available from a clinical CT scanner as many clinical scanners generate only the reconstructed CT images[7]. Additionally, projection-domain decomposition requires exact angular matching of the projections, which may be difficult on dual-source CT scanners[37]. This research focuses on image-domain decomposition, which is readily implementable on different CT scanners as a post-reconstruction procedure.

The fundamental limitation of quantitative DECT is significant noise amplification during the decomposition process and thus a decrease in signal-to-noise ratio.

Image-domain decomposition operates under the assumption that the linear attenuation coefficient is approximated by a linear combination of two basis functions. We can assume that position of the objects within the high and low energy images are constant, and thus each pixel will have two values for attenuation coefficient. The formulation of material decomposition is as follows:

$$\vec{\mu} = A\vec{x} \tag{2}$$

or,

$$\begin{pmatrix}\vec{\mu}_H \\ \vec{\mu}_L\end{pmatrix} = \begin{pmatrix}\mu_{1H}I & \mu_{2H}I \\ \mu_{1L}I & \mu_{2L}I\end{pmatrix}\begin{pmatrix}\vec{x}_1 \\ \vec{x}_2\end{pmatrix} \tag{3}$$

where $\vec{\mu}_H$ and $\vec{\mu}_L$ are the vectorized high and low energy images, each of length *N*, the total number of image pixels, and $\vec{x}_1$ and $\vec{x}_2$ are the unitless basis material images, containing the relative fractions of each material, and also of length *N*. μ_{1H}, μ_{2H}, μ_{1L}, μ_{2L} are the linear attenuation coefficients of materials 1 and 2 at high and low energies, and I is an *N*-by-*N* identity matrix. Solving for $\vec{x}$ yields the direct decomposition:

$$\vec{x} = A^{-1}\vec{\mu} \tag{4}$$

where A^{-1} is the decomposition matrix and is defined as:

$$A^{-1} = \frac{1}{\det(A)}\begin{pmatrix}\mu_{2L}I & -\mu_{2H}I \\ -\mu_{1L}I & \mu_{1H}I\end{pmatrix} \tag{5}$$

In the diagnostic energy range, the low and high energy spectra have great amounts of overlap. This means there is a relatively small difference in the attenuation coefficients at low and high energies, leading to a high condition number on the composition matrix *A*. Because of this, direct decomposition significantly amplifies noise[18]. As such, the

decomposition is very sensitive to noise on the initial CT images and material images can be difficult to interpret without noise suppression.

2.4.1 Noise Amplification in DECT

A characteristic of the bremsstrahlung photon beams used in CT is a continuous spectrum which is shifted to lower energies, with the peak typically at $E_0/3$, where E_0 is the max photon energy. This leads to large amounts of overlap between photon spectra even at different energies, shown in Fig. 12 for 75 kVp and 125 kVp spectra. Because the mean energies of beams are not highly different, the measured attenuation coefficient values of the low and high energy images are close in value, leading to a high condition number on the composition matrix A. Petrongolo et al used singular value decomposition to show that the condition number of A is proportional to the degree of noise amplification[18]. Additionally, because of the formulation of decomposition via matrix inversion, each material image will carry the sum of the noise variances of each CT image, and the signal within decomposed images becomes $(\mu_H\mu_{2L} - \mu_L\mu_{2H})$ or $(-\mu_H\mu_{1L} + \mu_L\mu_{1H})$. This leads to large signal cancellation, which, when coupled with summation of noise variances, results in a noise boost.

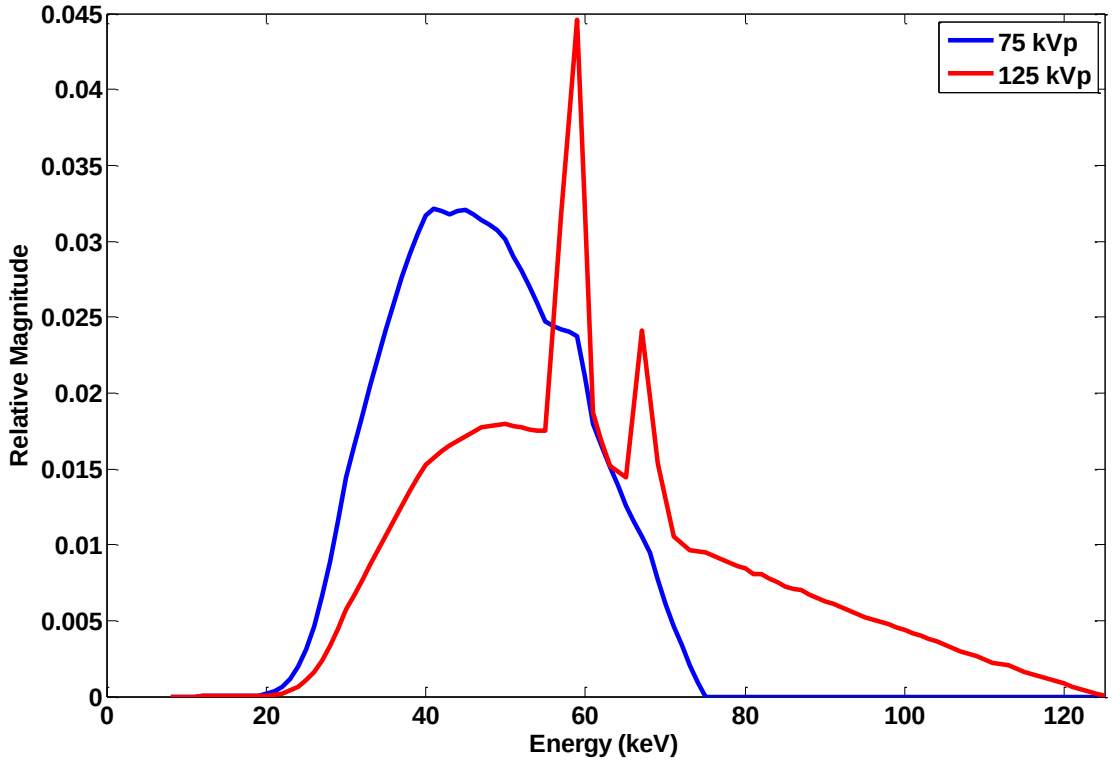

Figure 12. Spectra of 75 kVp and 125 kVp x-ray beams with 6 mm Al filtration.

2.5 Noise Power Spectrum

The standard deviation (STD) or variance of pixel values is commonly used to quantify the noise level of the image. While these quantities allow for comparisons of the amount of noise present in an image, they reveal no information about the noise characteristics. Boedeker et al showed that even in images with the same noise STD, the detectability of lesions can be vastly different[38, 39], as shown in Fig. 12.

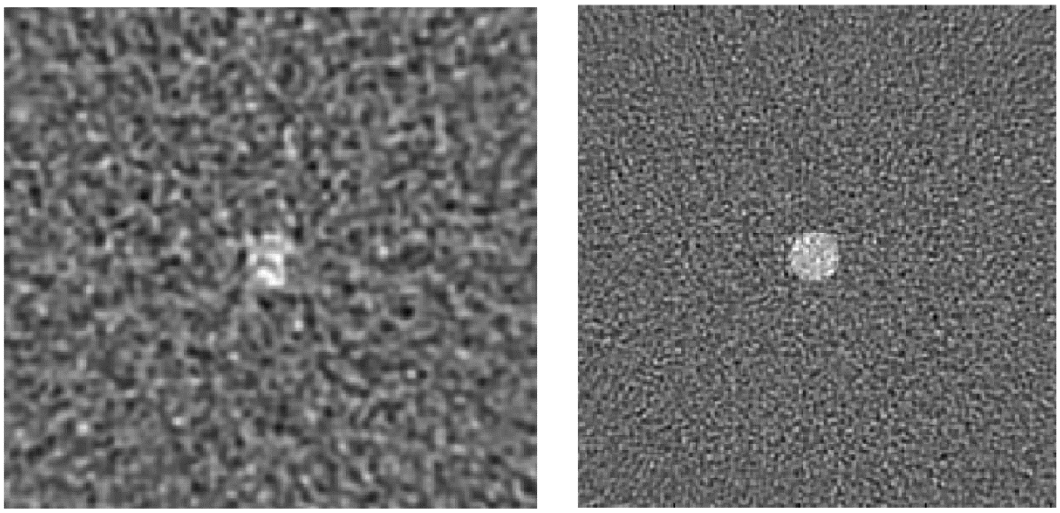

Figure 13. 2 mm slice of a sphere. The standard deviation in (a) and (b) is the same, however the graininess of the noise allows the lesion to be more easily detected in (b)[38].

To more fully characterize the behavior of noise, Reiederer et al developed the formulation for the noise power spectrum (NPS) in CT[40]. The NPS is calculated as the square of the discrete Fourier transform of the image noise, and is described more fully in section 3.5.

The NPS serves as a measure of the randomness of the noise at each spatial frequency[39]. In his initial paper discussing the formulation of NPS, Riederer showed that the variation in CT number is not random and has a correlation to the variation at other points in the image. NPS fully describes this phenomena, attributing the noise correlation to the filter used in image reconstruction by filtered backprojection (FBP)[40, 41], an example is shown in Fig. 14.

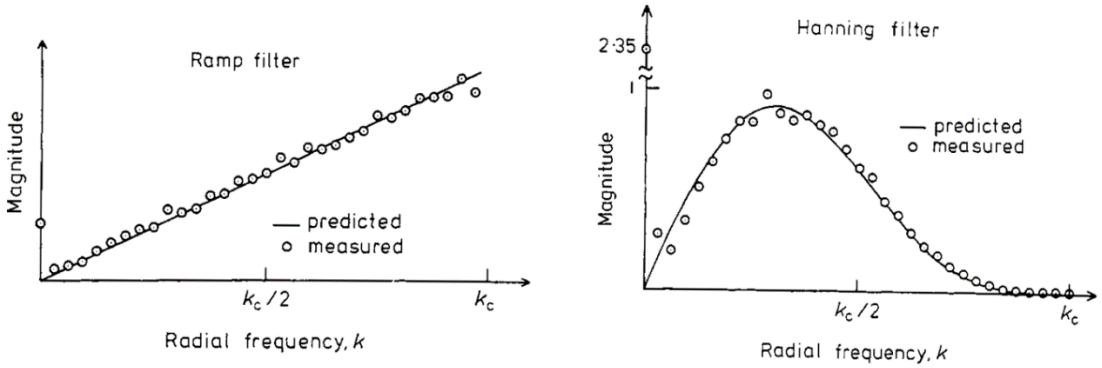

Figure 14. NPS of a CT image reconstructed via FBP with ramp filtering (left) and Hanning filtering (right). Taken from Ref. [40]

Typical noise suppression methods aim to decrease the variation between neighboring pixels, reducing the total image noise. While this successfully reduces noise STD, it preferentially suppress high frequency noise, leading to an altered image quality and NPS. The method developed in this research is designed to maintain the characteristics of the NPS of the CT image.

2.6 Existing Noise Suppression Methods

The problem of noise amplification has been known since the advent of DECT[20, 42-44], leading to the development of several noise suppression algorithms[21, 44-49]. Additionally, many algorithms from general image processing have been applied to DECT. Early on, Rutherford et al suppressed noise by using a 5-by-5 low-pass filter[47]. Denoising

methods such as this are simple to implement, however they result in degraded spatial resolution.

Several noise suppression methods specific to DECT have been proposed. Warp and Dobbins proposed evoking the structural redundancy provided by two images, smoothing only the high energy image before decomposition to prevent blurring of calcifications on the low energy image[45]. Kalendar et al first proved that the noise on material images is anti-correlated. They then exploited the anti-correlation between the two material images created during decomposition to design a noise suppression algorithm[44]. Macovski et al filtered both images, combining a low-pass filtered version of a "tissue" image and a high-pass filtered version of a "bone" image to produce a high SNR image[50]. Dong et al developed a method which combines the image reconstruction with image decomposition[51].

Niu et al recently proposed a new noise suppression algorithm for DECT which is based on both redundant structural information and the statistical nature of the decomposition process[19]. The authors use a penalized weighted least-square optimization, with the inverse of the variance-covariance matrix of the CT images as the penalty weight. Using the penalty weight for decomposition not only increases the accuracy of the noise suppression, it forces decomposition to be carried out iteratively. The method is further controlled by a regularization term, which aims to preserve edges of the initial CT images on the decomposed material images. The method, referred to as penalized weighted least-square optimization with edge-preserving regularization (PWLS-EPR), is distinct from other approaches in that the decomposition is carried out iteratively at the same time as noise suppression, leading to higher accuracy.

While PWLS-EPR effectively achieves noise reduction on DECT decomposed images, it does not utilize all of the structural information contained in the original CT images. The calculation of image gradient in the edge-preservation regularization means that only the pixels lying on or near material edges are used for regularization of the noise suppression. The noise is then decreased by reducing the variation between neighboring pixels, and the regularization contains no information on the image texture or quality. This inevitably degrades the image noise power spectrum (NPS), resulting in artificial or over-smoothed image textures[38, 39].

Chapter 3 - Method

3.1 Algorithm Design Goals

The goal of this research is to design a noise suppression algorithm which can achieve the following four goals: noise suppression by at least one order of magnitude while preserving both NPS and spatial resolution and maintaining accurate material density calculation. To achieve this, we aim to utilize the penalized weight least squares optimization framework, however with a different means of regularization. Rather than relying solely on edge pixels, we calculate the similarity between several pixels across an entire image. Based on the fact that averaging pixels of the same or similar materials gives a low-noise image, we include a regularization term in the objective of the optimization framework to minimize the difference between the images without and with noise suppression via averaging pixels of similar materials. The improved method is referred to as penalized weighted least-square optimization with similarity-based regularization (PWLS-SBR). Performance of PWLS-SBR on spatial resolution, DECT decomposition accuracy, and image NPS preservation is evaluated on the Catphan©600 phantom, an anthropomorphic head phantom, and a head-and-neck patient scan.

3.2 Iterative Image Domain Decomposition with Noise Suppression

Following is a review of the algorithm of iterative image-domain decomposition with noise suppression, i.e., PWLS-EPR[19]. As shown in previous studies[52], least square estimation with smoothness regularization can be used to suppress image noise. If this method of noise suppression is applied to material images, the formulation is:

$$\min_{x}(\vec{x} - A^{-1}\vec{\mu})^{T}(\vec{x} - A^{-1}\vec{\mu}) + \lambda\, R(\vec{x}) \tag{6}$$

where $R(\vec{x})$ is the regularization term to force smoothness of $\vec{x}$; $\vec{x}$, $\vec{\mu}$, and A^{-1} are as defined above; and λ is a parameter used to control the level of noise suppression. Eqn. (5) operates under the assumption that the noise on each pixel of $A^{-1}\vec{\mu}$ is independent, which is invalid for DECT since the noise is highly correlated[44].

The PWLS-EPR algorithm restructures Eqn. (6) based on the design principle of a best-linear unbiased estimator[53], including the inverse of the estimated variance-covariance matrix of the decomposed images as the penalty weight for the least-squares method. The optimization framework then takes the form:

$$\min_{\vec{x}} F(\vec{x}) = (A\vec{x} - \vec{\mu})^{T}V^{-1}(A\vec{x} - \vec{\mu}) + \lambda\, R(\vec{x}) \tag{7}$$

with matrix V defined as:

$$V = diag\left(var(\overrightarrow{n_{H1}}), \dots, var(\overrightarrow{n_{HN}}), var(\overrightarrow{n_{L1}}), \dots, var(\overrightarrow{n_{LN}})\right) \tag{8}$$

where $var(\overrightarrow{n_{Hi}})$ and $var(\overrightarrow{n_{Li}})$ are the estimated noise variances on the *i*'th pixel in the high-energy and the low-energy CT images. In our implementations, we measure the noise variance inside a small uniform area on the CT images and assume a stationary noise

distribution across the entire field of view. The second term preserves edges in the noise suppressed images, and is defined as:

$$R(x) = \frac{1}{2}\sum_{i}\sum_{k\in N_i} e_{ik}(\vec{x}(i) - \vec{x}(k))^2 \tag{9}$$

where N_i is the set of four neighbors of the i'th pixel in the image and e_{ik} is the edge weight. For edge weighting, the Canny method[54], which detects local maxima of the gradient after smoothing by a Gaussian kernel, is followed by the Prewitt method[55], which approximates the directional derivative and determines edges where the gradient is at a local maximum. The algorithm first detects edge pixels on the initial CT images and then assigns low values to e_{ik} only when either the i'th or the k'th pixel is on the edge. Such a regularization term allows sharp signal transition at edges, forcing the image to be piecewise constant and preserving edge structures on the decomposed material images.

The key result of this method is that it carries out the decomposition iteratively in step with noise suppression. Because the two tasks are carried out simultaneously, the composition matrix, *A*, is used at every iteration, which increases optimization accuracy. Additionally, PWLS-EPR fully utilizes the statistical characteristics of the decomposition.

3.3 Penalized Weighted Least-Square Optimization with Similarity-Based Regularization

Although PWLS-EPR fully exploits the statistical nature of the decomposed material images, the edge preservation regularization is based solely on edge pixels rather than the entire structural information contained in the initial CT images.

PWLS-SBR improves over PWLS-EPR by avoiding the gradient calculation in the regularization term. Note that, the true value of one image pixel, $\vec{x}(i)$, can be estimated via weighted averaging pixels of the same or similar materials, $\vec{x}(k)$, i.e.:

$$\langle \vec{x}(i) \rangle = \sum_{k \in N_i} w_{ik} \vec{x}(k) \tag{10}$$

where N_i are the pixels of the same or similar materials compared to the *i'*th pixel and w_{ik} is the normalized weight quantifying the similarity between the materials of the *i'*th and the *k'*th pixels, calculated from the values of the initial CT images. We discuss the calculation of w_{ik} later in the paper for the clarity of writing. Converting the above equation to a matrix form, one obtains:

$$\langle \vec{x} \rangle = W\vec{x} \tag{11}$$

where w_{ik} is the element of the similarity matrix W at the *i'*th row and the *k'*th column.

Eqn. (10) indicates that multiplying the image vector by the similarity matrix reduces the image noise. The difference between $\langle \vec{x} \rangle$ and $\vec{x}$ becomes smaller when $\vec{x}$ contains less noise. As such, if $\vec{x}$ is the result of a successful noise suppression algorithm, the following approximation holds:

$$\vec{x} \approx W\vec{x} \tag{12}$$

Using Eqn. (12) as an additional data condition, the PWLS-SBR algorithm adopts the same optimization framework shown as Eqn. (7), but with a regularization term to ensure that Eqn. (12) is valid, i.e.:

$$\min_x F(\vec{x}) = (A\vec{x} - \vec{\mu})^T V^{-1} (A\vec{x} - \vec{\mu}) + \lambda ||W\vec{x} - \vec{x}||_2^2 \tag{13}$$

where matrix V is defined in Eqn. (8), $\|\cdot\|_2$ calculates the L-2 norm of a vector, and λ is still a user-defined parameter that controls the strength of noise suppression.

The calculation of w_{ik} or the similarity matrix W is critical to the performance of PWLS-SBR on noise suppression. In general, for each pixel i, we should include a large number of similar pixels in the calculation of w_{ik} so that the mean value of $\vec{x}(i)$ can be accurately calculated. In this research, inspired from the sigma filter[56, 57], we use an empirical Gaussian model. The similarity s_{ik} between pixels i and k is calculated as:

$$s_{ik} = \begin{cases} \exp\left(-\frac{(\vec{x}(i)-\vec{x}(k))^2}{h^2}\right), & if\ |\vec{x}(i)-\vec{x}(k)| < 3h\ and\ k \in \Omega_i \\ 0, & otherwise \end{cases} \quad (14)$$

where h is another user-defined parameter that controls the width of the Gaussian similarity window. In our implementations, we set h as the measured noise STD on the CT images. The search window, Ω_i, starts from a neighborhood of 41-by-41 pixels. If the number of neighboring pixels with non-zero s_{ik} values is less than 200, the size of search window automatically increases until the goal is reached or the search window is the entire image. This strategy ensures an adequate number of similar pixels for noise suppression. After normalization, the element of the similarity matrix is calculated as:

$$w_{ik} = \frac{s_{ik}}{\Sigma_k s_{ik}} \quad (15)$$

We use Eqns. (14) and (15) to calculate the similarity matrix in the PWLS-SBR algorithm based on the initial CT images. To reduce errors stemming from the CT image noise, we generate a first-pass similarity matrix from a noisy CT image, and suppress noise on the CT image by matrix multiplication shown in Eqn. (11). An updated similarity matrix is then produced on the noise-suppressed CT image. Furthermore, similarity matrices are calculated on the high-energy and the low-energy CT images separately, and averaged to generate a low-noise similarity matrix for use in PWLS-SBR.

3.4 Solver to PWLS-SBR

The objective function in Eqn. (13) is convex and differentiable. As such, the condition for the optimal solution is:

$$\nabla F(\vec{x}) = 0 \Longrightarrow (A^T V^{-1} A + \lambda \cdot \nabla R)\vec{x} = A^T V^{-1}\vec{\mu} \tag{16}$$

where ∇R is the gradient of the similarity-based regularization:

$$\nabla R = (\bar{W} - I)^T(\bar{W} - I)\vec{x} \tag{17}$$

Eqn. (16) can be solved using a pre-conditioned conjugate gradient method.

3.5 Evaluation

We compare PWLS-SBR to both decomposition via direct matrix inversion, i.e., Eqn. (4), and PWLS-EPR, i.e., Eqn. (7). As shown in the previous section, the penalty weight on the regularization term, λ, is the only tuning parameter for both algorithms of PWLS-SBR and PWLS-EPR. In the presented results, unless otherwise stated, we adjust λ values to achieve the same noise STD on the noise-suppressed images for fair comparisons.

Two physical phantoms are used in the evaluation studies, the Catphan©600 phantom (The Phantom Laboratory: Salem, NY) and an anthropomorphic head phantom. Projection data are acquired on our tabletop CT system at Georgia Institute of Technology. The geometry of the tabletop CT exactly matches that of the on-board imager of a Varian clinical linear accelerator. More description about the system can be found in Ref. 54[58]. To inherently reduce scatter contamination on projection data, a fan-beam geometry is used

and the illuminated area in the longitudinal direction on the detector has a width of 15 mm. Each CT scan contains 655 equi-angular projections, with 75 kVp and 125 kVp as the low and high tube energies and a tube current of 80 mA. CT images are reconstructed via FBP with an image size of 512-by-512 pixels and 0.5-by-0.5 mm^2 pixel size. Patient data for a head-and-neck scan, acquired with 80 kVp as the low tube energy and 140 kVp as the high tube energy, is also used for evaluation. All the algorithms are implemented in Matlab. The Matlab function *pcg* is used to solve Eqn. (16). PWLS-SBR typically takes 180 seconds, depending on the level of noise suppression, to process one CT dataset on a 2.79 GHz PC with 4.022 GB of physical memory.

Spatial resolution is evaluated using the line-pair slice of the Catphan©600 phantom consisting of aluminum line-pairs, ranging from a spatial frequency of 1 to 21 line pairs per cm. We use NPS to investigate the image quality difference for results from different algorithms at the same noise level[38, 39]. NPS is measured inside a uniform region of interest (ROI) as:

$$NPS = |DFT_2\{f\}|^2 \tag{18}$$

where f is the two-dimensional (2D) image inside the uniform ROI offset by its mean value and DFT_2 is the 2D discrete Fourier transform[39, 59, 60].

The slice of the Catphan©600 phantom containing contrast rods of various materials is used to assess decomposition accuracy via electron density measurement. Highly accurate electron density maps have become increasingly important in radiation therapy treatment planning for precise dose calculation[61]. The electron density is calculated from the decomposed material images as:

$$\rho_e = \rho_{e,b}\, x_b + \rho_{e,t} x_t \tag{19}$$

where x_b and x_t are the decomposed material images (i.e., relative fractions of basis materials), $\rho_{e,b}$ and $\rho_{e,t}$ are the corresponding electron densities of the basis materials. For each contrast rod, the percent error of electron density measurement is computed as:

$$E(\%) = \left(\frac{|\bar{\rho}_e - \rho_e^{ref}|}{\rho_e^{ref}} \right) \times 100\% \tag{20}$$

where ρ_e^{ref} is the true material electron density, as published in the Catphan©600 phantom manual, and $\bar{\rho}_e$ is the mean measured value inside each rod. The root-mean-square of the percent errors (RMSE) is calculated for all contrast rods to quantify the overall accuracy.

Patient data for a head-and-neck scan and an anthropomorphic head phantom are used to evaluate the method performance on objects with realistic and complex structures. On the head phantom, we choose a slice containing the intricate bony anatomy of the sinuses, a challenging case for noise suppression without losing fine structures. On the patient data, we show the method's performance on bone, soft tissue, and contrast-enhanced blood vessels.

Chapter 4 - Results

4.1 Catphan Study on Spatial Resolution and NPS

Fig. 15 shows the 75 kVp and 125 kVp CT images and Fig. 16 shows the results of material decomposition via direct matrix inversion without noise suppression, PWLS-SBR, and PWLS-EPR. Aluminum, the material of the line pairs, and epoxy, the material of the background, are chosen as basis materials for DECT decomposition, mimicking "bone" and "tissue", respectively, in a clinical setting. The mean and STD calculated inside the ROI indicated in the "tissue" image without noise suppression of Fig. 16 are shown in Table 1 for each material image. For fair comparisons, we have tuned algorithm parameters such that both PWLS-SBR and PWLS-EPR achieve the same noise STD reduction, a factor of more than one order of magnitude. The zoom-in inserts on Fig. 15 and Fig. 16 scrutinize the performance on image spatial resolution. It is seen that PWLS-SBR preserves a spatial resolution of 8 line pairs per cm in both the "bone" and "tissue" images, comparable to that of the initial CT images. While PWLS-EPR can preserve this resolution on the "bone" image, the line pairs are blurred out on the "tissue" image. Additionally, PWLS-EPR cannot preserve the high density value on the "bone" image. This is because the regularization term only includes information for pixels lying on the edge and noise suppression cannot preserve high intensity values in the interior of the rod. As the algorithm tries to smooth, it flattens the signal throughout the line-pair, bringing down the average value. Since the similarity method regularizes based on the whole material of the line-pair, it can preserve the high intensity value.

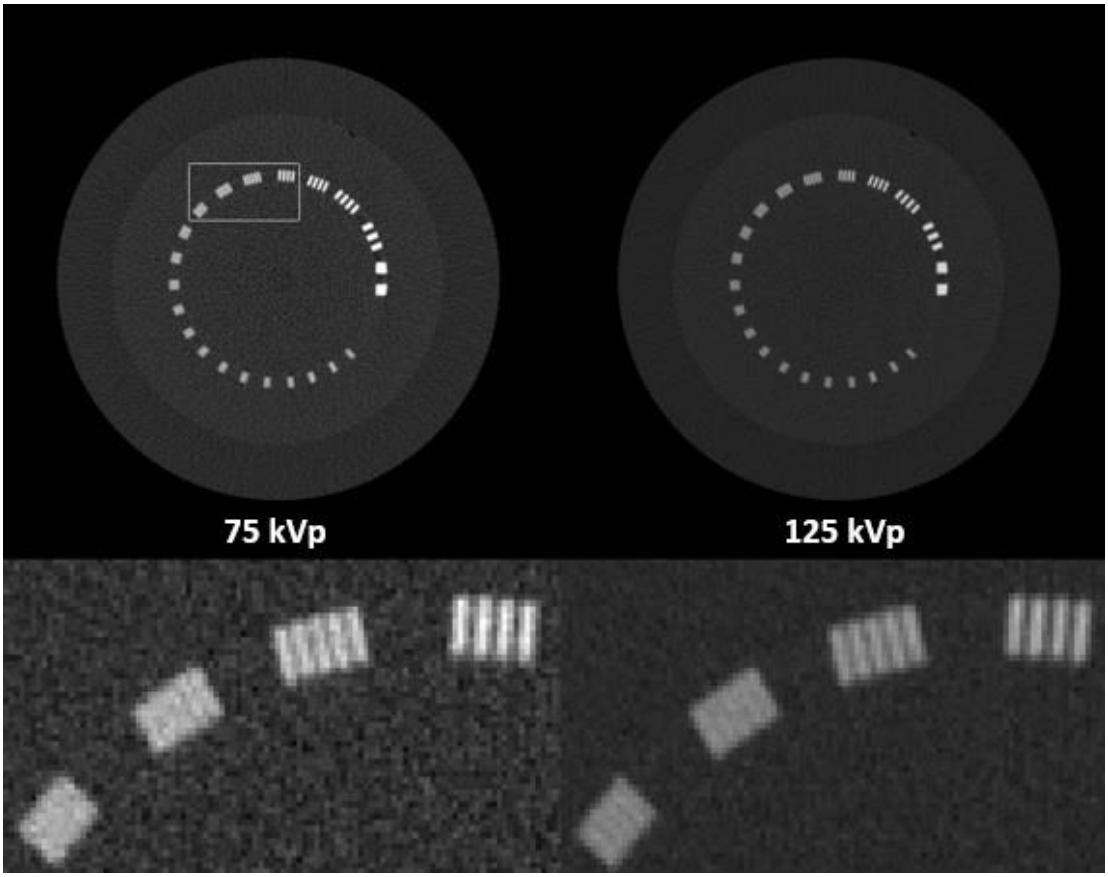

Figure 15. CT images of the line-pair slice of the Catphan©600 phantom. Display window: [-500 2500] HU.

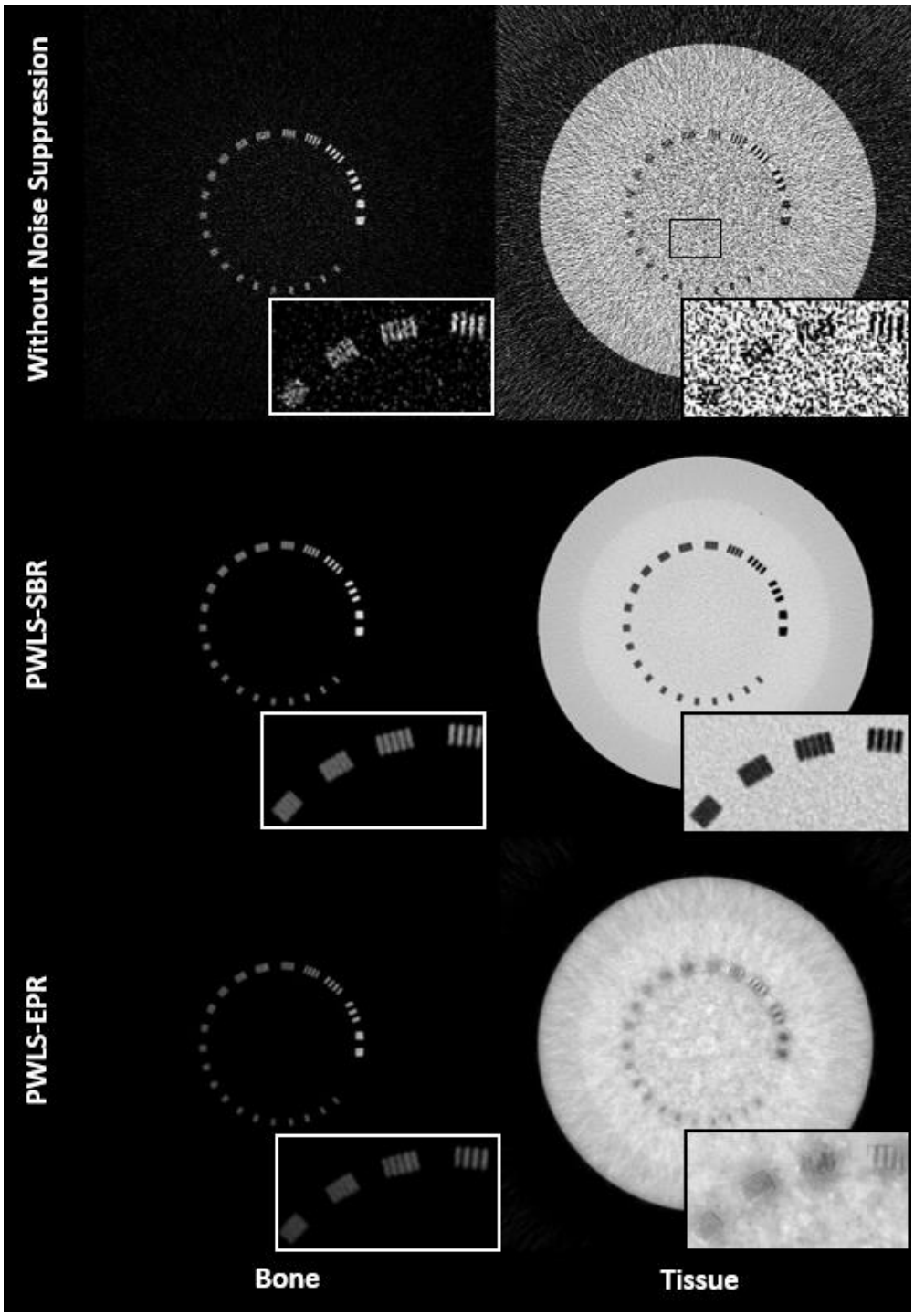

Figure 16. Decomposed “bone” and “tissue” images using direct matrix inversion without noise suppression, PWLS-SBR, and PWLS-EPR. The region where the inserts are taken is outlined on the low energy CT image in Fig. 15 and the ROI used to calculate mean and STD values of Table 1 is outlined on the “tissue” image without noise suppression. Display window: [0.2 1.2].

Table 1. The measured mean ± STD for each material image shown in Fig. 16. The ROI used in the calculation is indicated in the "tissue" image without noise suppression of Fig. 16.

	"Bone" Image	"Tissue" Image
Without Noise Suppression	0.01 ± 0.24	0.99 ± 0.74
PWLS-SBR	0.01 ± 0.02	0.99 ± 0.05
PWLS-EPR	0.00 ± 0.02	1.01 ± 0.05

In addition to the difference in spatial resolution, it can be clearly seen that PWLS-SBR and PWLS-EPR produce images with different textures despite having the same noise level (obvious especially on the "tissue" images of Fig. 16). This is due to the difference on image NPS as shown in Fig. 17. PWLS-EPR heavily suppresses high-frequency noise, while PWLS-SBR preserves the shape of the NPS distribution of direct decomposition without noise suppression. For a quantitative measure, we average the 2D NPS in the angular direction to reduce noise and plot 1D profiles of the averaged NPS in the radial direction shown in Fig. 18. Note that Parserval's theorem states that the total energy (i.e., sum of squares) in the signal domain equals that in the Fourier domain. Since the images of PWLS-SBR and PWLS-EPR have the same noise variance, their NPS have the same total energies. The NPS curve of direct decomposition without noise suppression is scaled down based on the noise reduction level to match the results of PWLS-SBR and PWLS-EPR. The NPS using PWLS-SBR has a correlation of 93% with that via direct decomposition (which has 96% correlation compared to the 75 kVp CT image), while the correlation drops to -52% for PWLS-EPR. The negative correlation of PWLS-EPR can be explained by the low frequency peak in the 1D-NPS, where no suppression produces a 1D-NPS with the peak shifted towards higher frequencies.

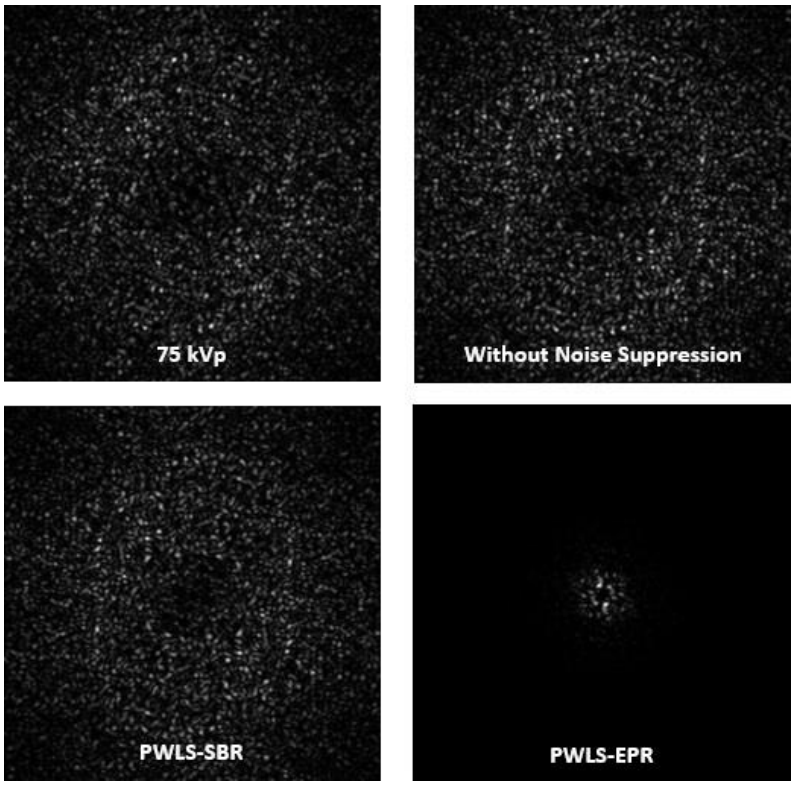

Figure 17. 2D NPS, calculated for a central region of 100-by-100 pixels of the line-pair "tissue" images, offset by its mean value. Display window [min max].

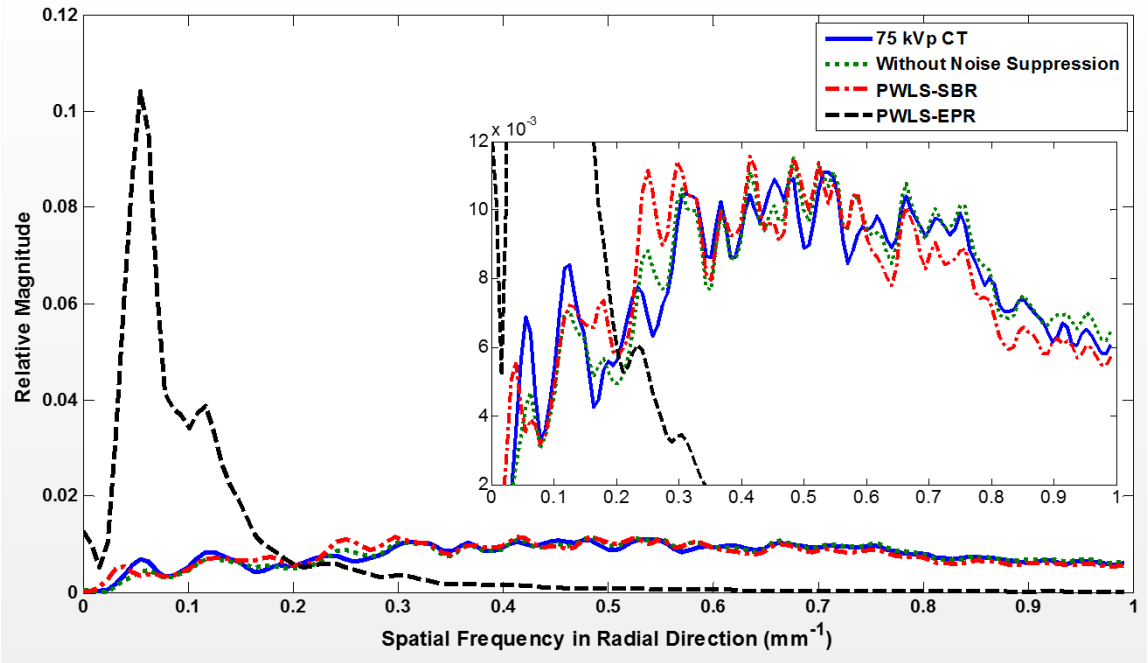

Figure 18. NPS in the radial direction after averaging in the angular direction for all images shown in Fig. 17.

4.2 Catphan Study on Electron Density

Fig. 19 shows the CT images of the contrast rod slice of the Catphan©600 phantom. Different materials used for electron density measurements are labeled on the 125 kVp CT image. Aluminum and low density polyethylene (materials 1 and 7) are used as the "bone" and "tissue" materials for decomposition. Fig. 20 shows both the material images (left two columns) and the electron density images (right column) via direct matrix inversion without noise suppression, PWLS-SBR, and PWLS-EPR. The parameters are tuned for very strong noise suppression, noise STD reduction by a factor of 13 for "bone" images and by a factor of 149 for "tissue" images, to demonstrate the high level of accuracy that can be maintained by PWLS-SBR. Table 2 contains mean values of electron densities measured within various rods. PWLS-EPR has an electron density RMSE of 2.21%, while PWLS-SBR further reduces the RMSE down to 1.20%. Additionally, it is obvious via visual inspection that PWLS-SBR achieves a much improved image quality on overall image uniformity and spatial resolution.

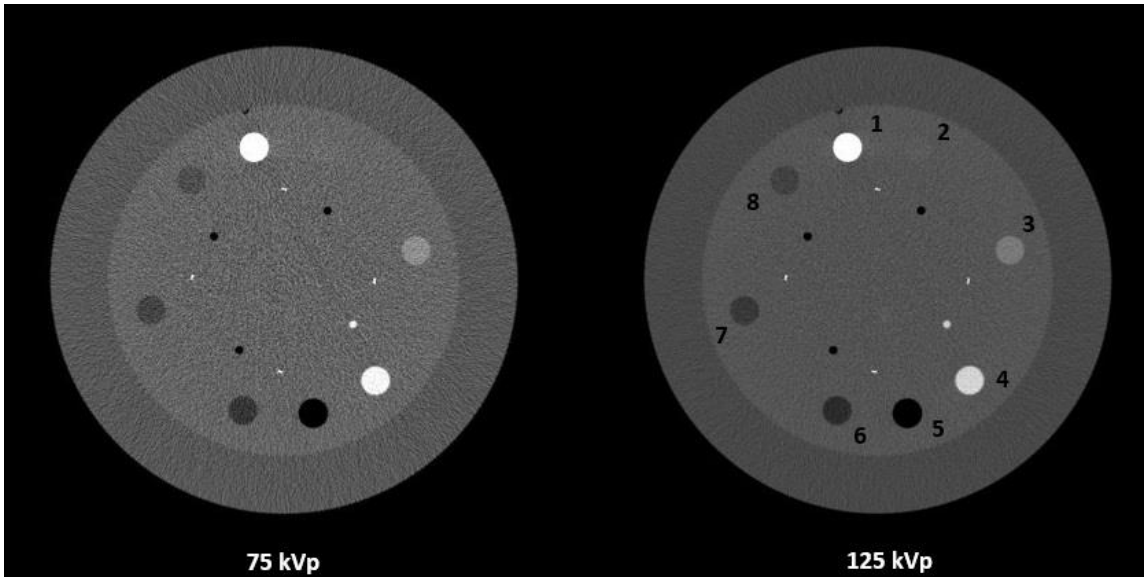

Figure 19. CT images of the contrast-rod slice of the Catphan©600 phantom. The numbered materials are: [1] aluminum, [2] acrylic, [3] Delrin, [4] Teflon, [5] air, [6] polymethylpentene, [7] low density polyethylene (LDPE), and [8] polystyrene. Display window: [-500 1000] HU.

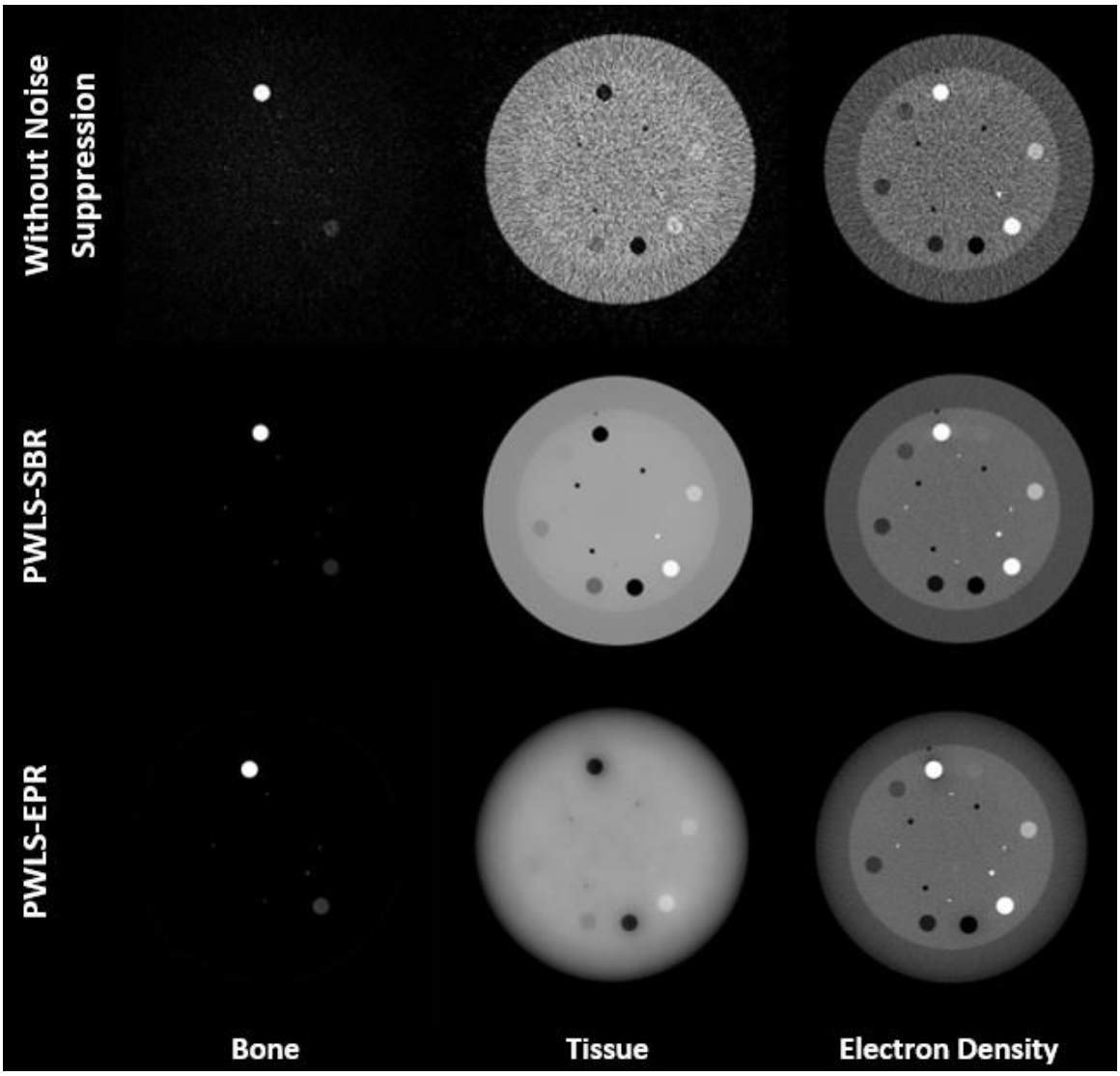

Figure 20. Material and electron density images of the contrast rod slice of the Catphan©600 phantom. Display windows are [0.1 0.7] for bone, [0.6 1.4] for tissue and [2.75 5] $\times 10^{23}$ e/cm^3 for electron density maps.

Table 2. The measured mean electron densities in unit of 10^{23} e/cm^3 for different contrast rods. The last column shows the overall RMSE.

	Alum-inum	Acrylic	Delrin	Teflon	PMP	LDPE	Poly-styrene	RMSE
Actual Electron Density	7.83	3.83	4.56	6.24	2.85	3.16	3.34	
Without Noise Suppression	7.81	3.82	4.40	5.91	2.86	3.15	3.33	0.91%
PWLS-SBR	7.75	3.76	4.34	5.86	2.89	3.20	3.39	1.20%
PWLS-EPR	8.86	3.75	4.29	5.70	2.98	3.24	3.38	2.21%

4.3 Anthropomorphic Head Phantom Study

The anthropomorphic head phantom contains a calcium-based substance and an epoxy to mimic bone and soft tissue, respectively, which are used as the basis materials in DECT decomposition. Fig. 21 shows the low and high energy CT images of a slice of the anthropomorphic head phantom. Fig. 22 shows the results of material decomposition via direct matrix inversion without noise suppression, PWLS-SBR, and PWLS-EPR. The mean and STD values measured in the ROI indicated by a black rectangle in Fig. 22 are listed in Table 3. Both PWLS-SBR and PWLS-EPR achieve the same level of noise STD reduction, i.e., by a factor of 24 and 57 on "bone" and "tissue" images, respectively. Again, it is clear that the texture of the original image is preserved by PWLS-SBR and high frequency noise is over-suppressed by PWLS-EPR. Fig. 23 allows for a closer examination of the fine sinus structures. These structures are buried in noise in the result of direct

decomposition. It is seen that PWLS-SBR better preserves the structures present on the initial CT images than PWLS-EPR.

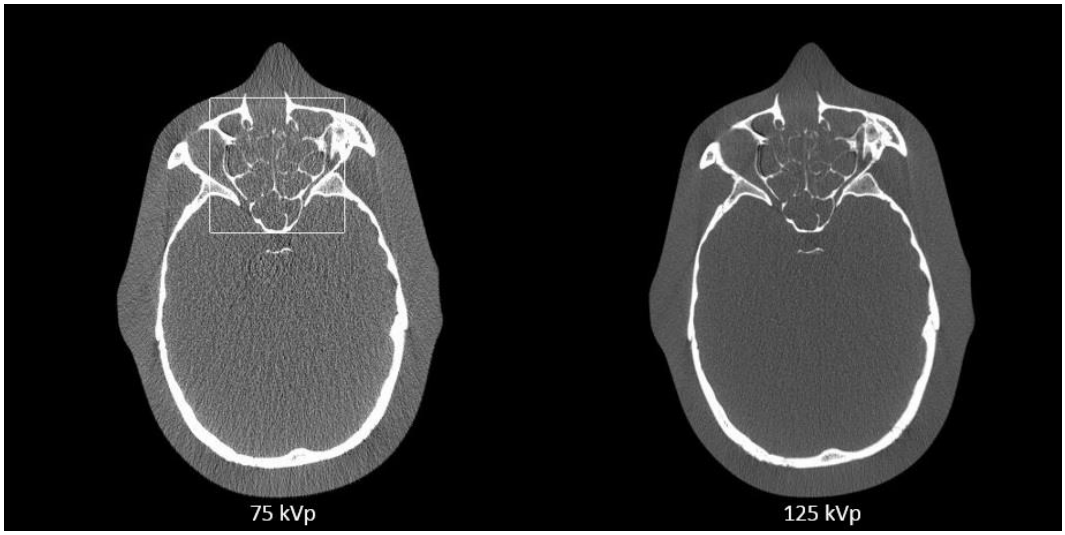

Figure 21. CT images of the anthropomorphic head phantom. The white box on the 75 kVp image outlines the insert region shown in Fig. 23. Display window: [-500 1000] HU.

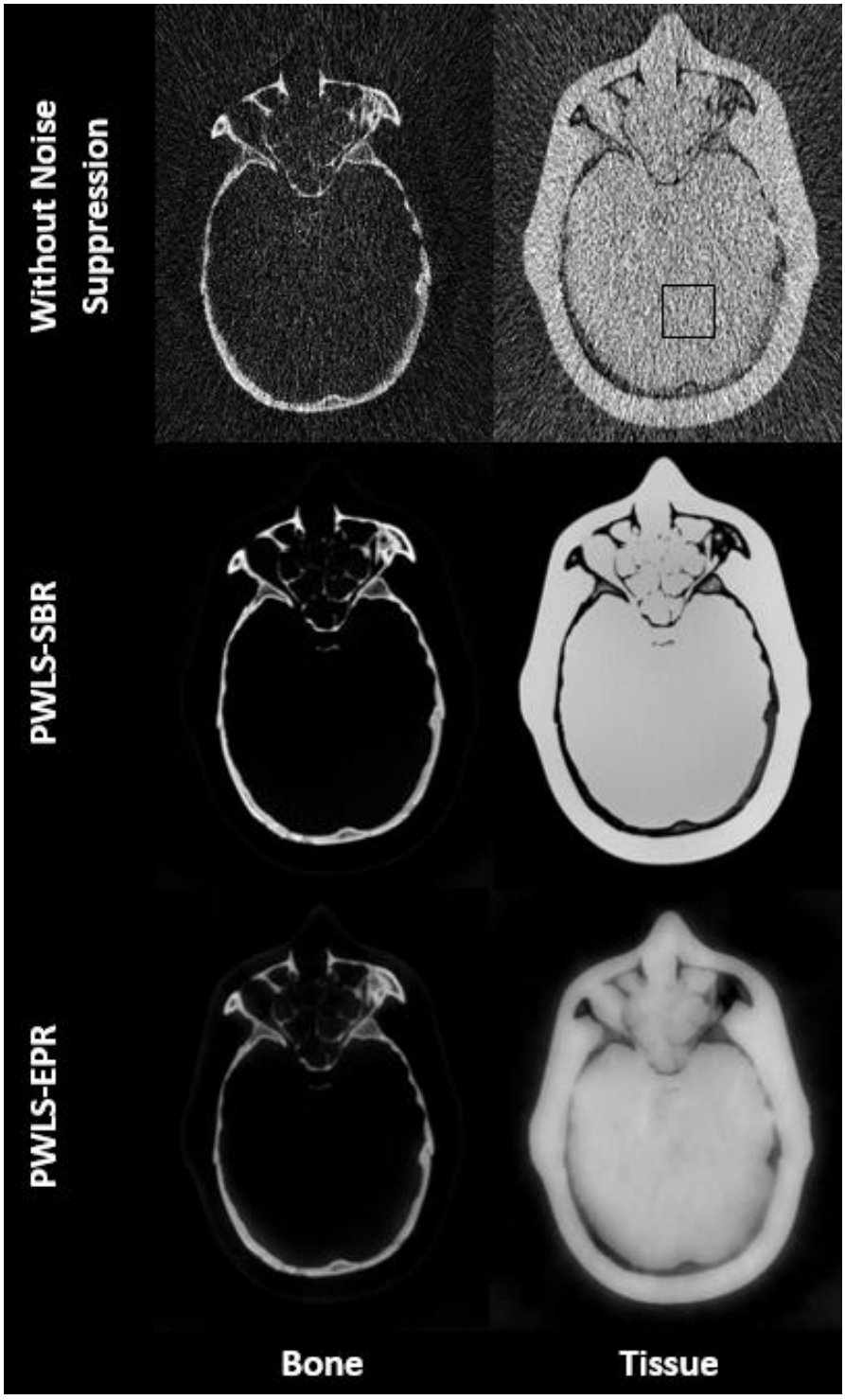

Figure 22. Decomposed material images of the anthropomorphic phantom using direct decomposition without noise suppression, PWLS-SBR and PWLS-EPR. The black rectangle indicates the ROI where the mean and STD values are calculated in Table 3. Display window [0.01 1.4].

Table 3. Mean ± STD measured on the images shown in Fig. 22, where the black rectangle indicates the ROI used in the calculation.

	"Bone" image	"Tissue" image
Without Noise Suppression	0.00 ± 0.54	1.00 ± 1.21
PWLS-SBR	-0.01 ± 0.02	1.01 ± 0.02
PWLS-EPR	-0.01 ± 0.02	1.01 ± 0.02

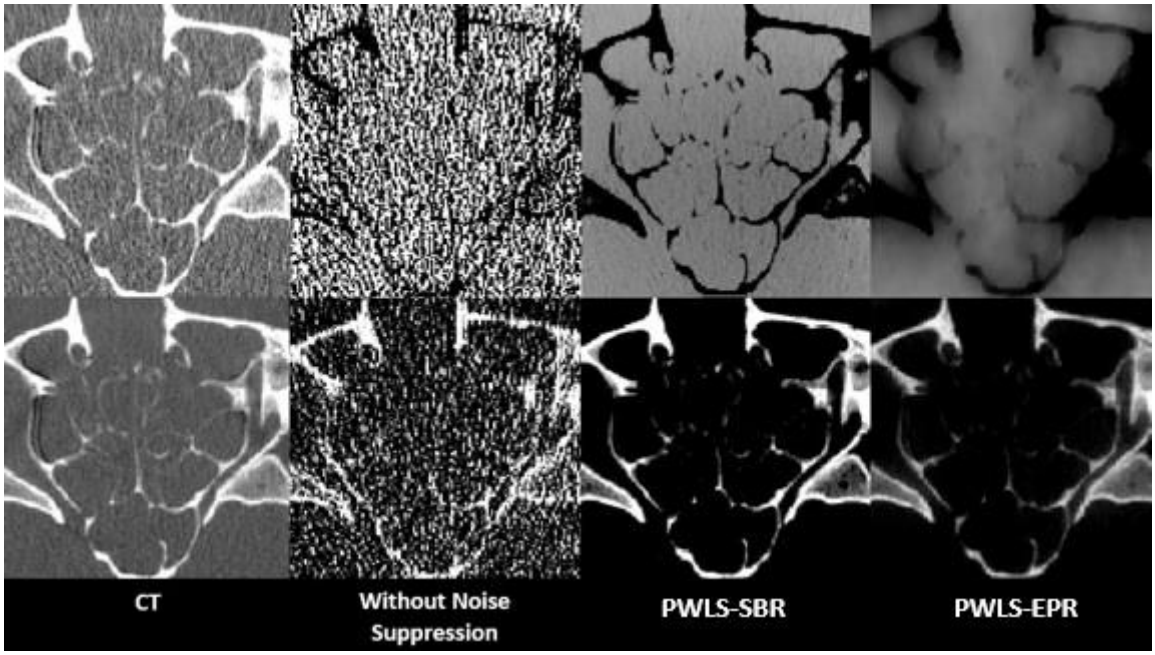

Figure 23. Zoom-in images of the sinus region for all images shown in Figs. 21 and 22. CT images display window: [-500 1000] HU, "bone" images display window: [0.1 1.0], and "tissue" images display window: [0.6 1.4].

4.4 Evaluation on Patient Data

For further evaluations of realistic anatomical structures, we choose to compare PWLS-SBR to PWLS-EPR and direct matrix inversion on data for a head-and-neck patient, with the CT images shown in Fig. 24. A region of the jaw was used to define the bone material, and a region of muscle tissue in the patient's posterior was used to define the tissue material. Table 4 shows the mean ± STD for the ROI indicated in Fig. 25. Both PWLS-SBR and PWLS-EPR achieve the same level of noise STD reduction, i.e., by a factor of 4 and 5 on "bone" and "tissue" images, respectively. Because the effective energies for this scan were further apart (80 kVp and 140 kVp vs. 75 kVp and 125 kVp), this image decomposition yielded lower initial noise levels, and thus required less noise suppression. Fig. 25 shows the results of material decomposition via direct matrix inversion without noise suppression, PWLS-SBR, and PWLS-EPR. The mean and STD values measured in the ROI indicated by the black rectangle in Fig. 25. PWLS-SBR is able to achieve a higher quality image than PWLS-EPR. PWLS-SBR performs exceptionally well on this image, preserving all the fine structures, as seen in Figs. 26 and 27, which show the "bone" image in red overlaid on the 80 kVp CT image.

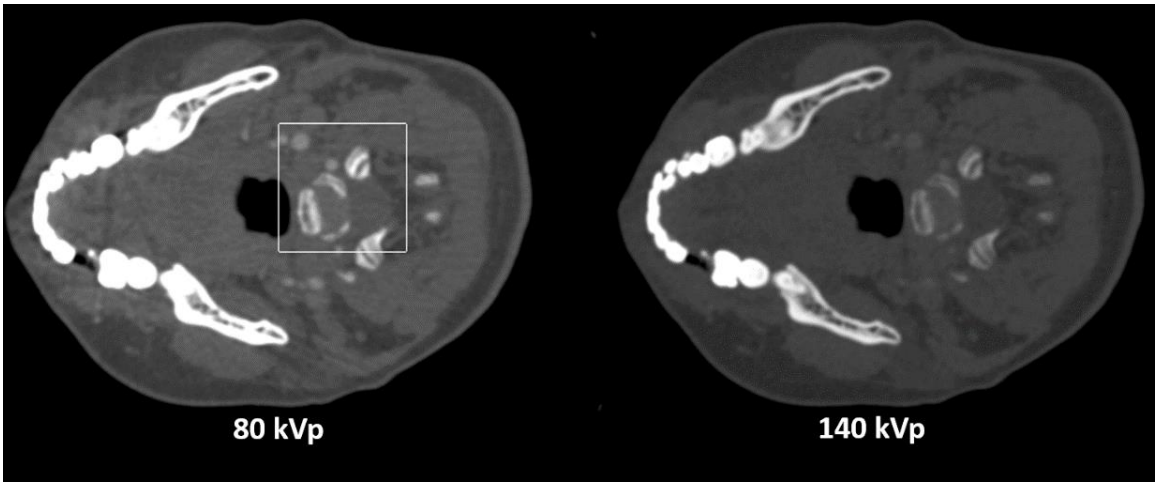

Figure 24. CT images of a head-and-neck patient. The white box on the 80 kVp image outlines the insert region shown in Fig. 25. Display window: [-500 1000] HU.

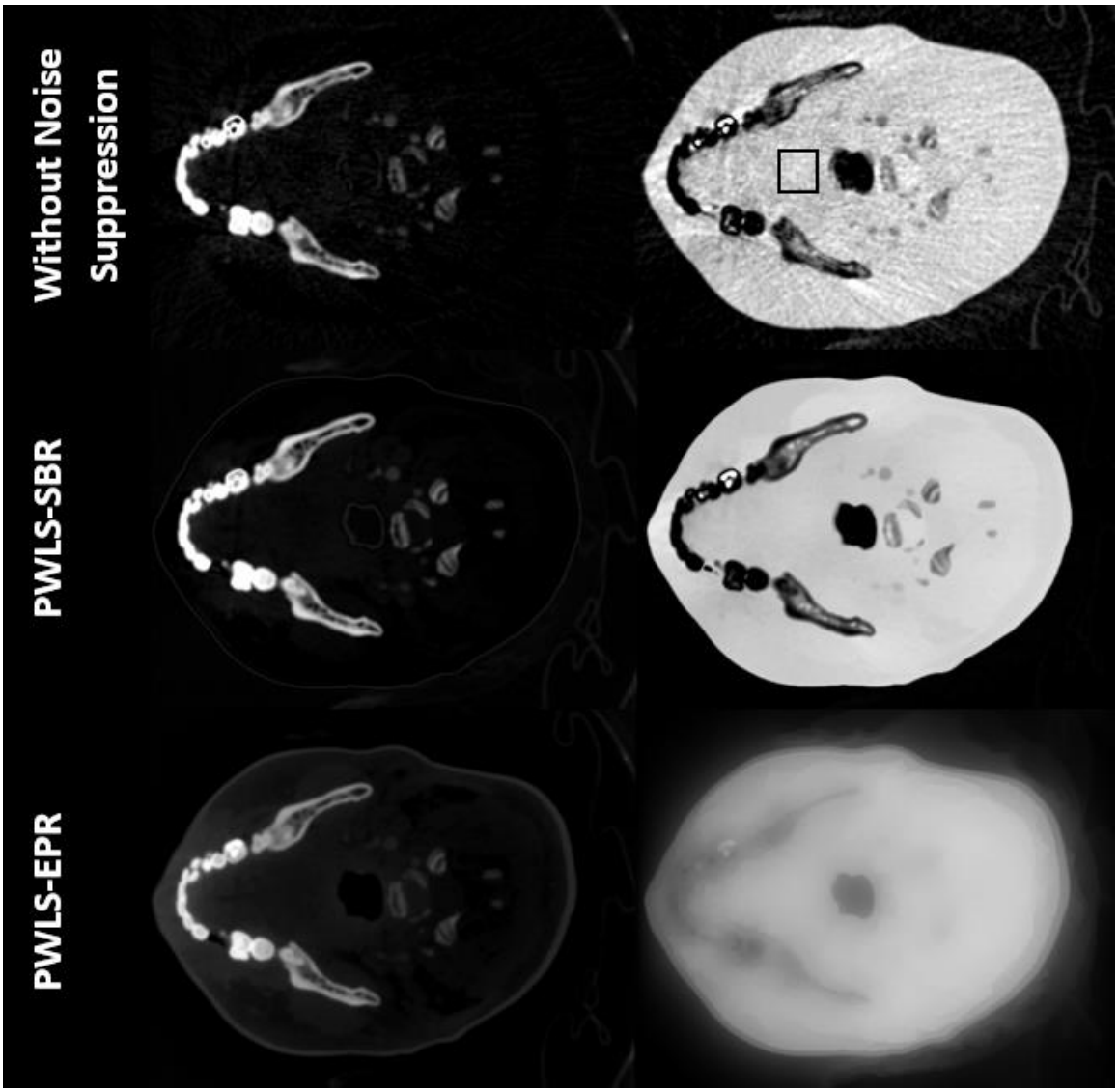

Figure 25. Decomposed bone and tissue images using direct matrix inversion without noise suppression, PWLS-SBR, and PWLS-EPR. The ROI used to calculate mean and STD values of Table 4 is outlined on the tissue image without noise suppression. Display window: [0 1.2].

Table 4. Mean ± STD of all of the images shown in Fig. 24, where the black rectangle indicates the ROI used in calculation.

	"Bone" Image	"Tissue" Image
Without Noise Suppression	0.04 ± 0.03	0.96 ± 0.03
PWLS-SBR	0.04 ± 0.01	0.94 ± 0.01
PWLS-EPR	0.04 ± 0.01	0.86 ± 0.01

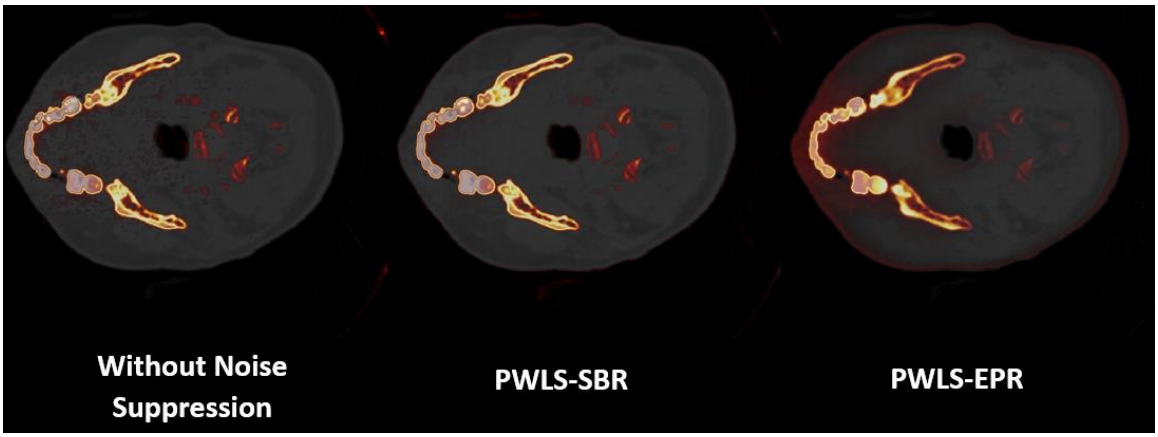

Figure 26. 80 kVp CT image with "bone" image overlaid in orange.

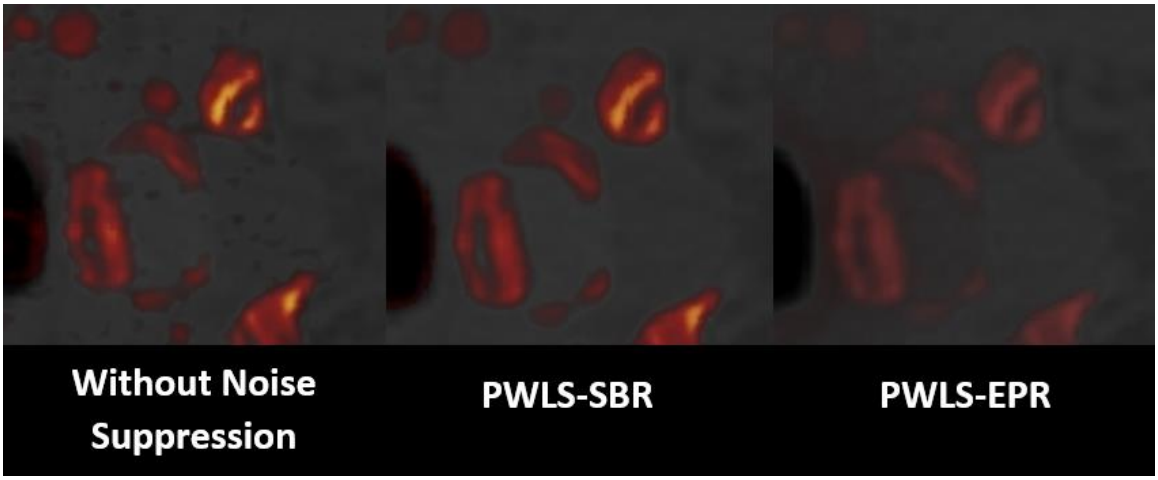

Figure 27. Zoom in images of the 80 kVp CT image overlaid with bone images (orange), region outlined in Fig. 10.

Chapter 5 - Discussion

In this research, we improve a previously developed noise suppression method, PWLS-EPR[19], for DECT decomposition by designing a new regularization term. PWLS-EPR includes gradient calculation in the regularization for edge preservation, and therefore fails to preserve the NPS of the original image after noise suppression. The proposed PWLS-SBR algorithm adopts regularization that extracts the entire redundant structural information contained within the two initial CT images. Phantom studies show that, at a high noise STD reduction level (a factor of more than one order of magnitude), PWLS-SBR maintains both image spatial resolution (up to 8 lp/cm) and NPS (>90% correlation) comparable to that of the initial CT image, a clear advantage over PWLS-EPR. In addition, PWLS-SBR reduces the RMSE of electron density measurement from 2.21% using PWLS-EPR down to 1.20%.

The similarity-based regularization in PWLS-SBR stands on the establishment of a new data condition, i.e., Eqn. (12), which uses a large number of similar pixels for noise suppression on one pixel. In our implementations, we choose to calculate the similarity matrix W using an empirical Gaussian model. Other more sophisticated algorithms of similarity matrix calculation are expected to achieve similar or even improved performance of PWLS-SBR, as long as Eqn. (12) holds and each row of W has a large number of non-zero elements (i.e., the number of similar pixels is sufficient). For example, one may find similar pixels to one pixel using image segmentation, and assign equal similarity to all these pixels. Furthermore, although we focus our paper on linear image-domain decomposition of DECT, the proposed method is readily translatable to non-linear

projection-domain decomposition, using the same technique as shown in our recent paper[62].

The PWLS-SBR algorithm has two indications beyond the scope of DECT imaging. First, our results reveal that the similarity-based regularization is superior in preservation of image NPS compared with gradient-based regularization, although the latter is widely used for retaining edges during noise suppression. Following similar derivations of this paper, we can design similarity-based regularization for noise suppression in other imaging scenarios with improved image NPS. Secondly, the similarity matrix is able to extract structural information from one image for reducing noise on images with different intensities but the same structures. As such, with different formations of similarity matrices, PWLS-SBR can be used for noise suppression with prior images from the same imaging device but with different settings or even from different imaging modalities. For example, in energy-resolved CT imaging, we can calculate the similarity matrix on the image from one energy channel, and use PWLS-SBR for noise suppression on the images from all other energy channels. The similarity matrix can even be calculated on an MRI image for noise suppression on a CT image of the same patient, as long as the two images are well registered and have exactly matching structures.

Chapter 6 – Conclusions

Dual-energy CT provides a diagnostic advantage over CT alone in its ability to extract information on the chemical composition of the materials in the image. This process, called basis material decomposition, yields significant noise amplification and decrease in the signal to noise ratio (SNR) of material images. Many noise suppression methods have been developed for and applied to DECT. However, noise suppression typically relies on reducing the signal variation from pixel to pixel. To keep the sharp edges present in the image, noise suppression is usually regulated based on the image gradient. While the gradient contains edge information, it does not provide any information on the texture of the image. Gradient-based noise suppression algorithms are prone to over-smoothing artifacts, leading to degradation of the original image quality. Our method preserves image quality by avoiding gradient calculation, and instead uses a pixel similarity-based regularization. By including every pixel in the regularization, the image texture can be preserved.

REFERENCES

1. Alvarez, R.E. and A. Macovski, *Energy-selective reconstructions in X-ray computerised tomography.* Physics in Medicine and Biology, 1976. **21**(5): p. 733.

2. Li, Y., et al., *Iodine quantification with dual-energy CT: phantom study and preliminary experience with VX2 residual tumour in rabbits after radiofrequency ablation.* The British Journal of Radiology, 2013. **86**(1029): p. 20130143.

3. Chandarana, H., et al., *Iodine quantification with dual-energy CT: phantom study and preliminary experience with renal masses.* American Journal of Roentgenology, 2011. **196**(6): p. W693-W700.

4. Primak, A.N., et al., *Noninvasive Differentiation of Uric Acid versus Non–Uric Acid Kidney Stones Using Dual-Energy CT.* Academic Radiology, 2007. **14**(12): p. 1441-1447.

5. Graser, A., et al., *Dual energy CT characterization of urinary calculi: initial in vitro and clinical experience.* Investigative radiology, 2008. **43**(2): p. 112-119.

6. Eiber, M., et al., *Targeted dual-energy single-source CT for characterisation of urinary calculi: experimental and clinical experience.* European Radiology, 2012. **22**(1): p. 251-258.

7. Yu, L., S. Leng, and C.H. McCollough, *Dual-Energy CT–Based Monochromatic Imaging.* American Journal of Roentgenology, 2012. **199**(5_supplement): p. S9-S15.

8. Yuan, R., et al., *Reduced Iodine Load at CT Pulmonary Angiography with Dual-Energy Monochromatic Imaging: Comparison with Standard CT Pulmonary Angiography—A Prospective Randomized Trial.* Radiology, 2012. **262**(1): p. 290-297.

9. Wu, X., et al. *Monochromatic CT image representation via fast switching dual kVp.* in *SPIE Medical Imaging*. 2009. International Society for Optics and Photonics.

10. Thieme, S.F., et al., *Dual Energy CT lung perfusion imaging—Correlation with SPECT/CT.* European Journal of Radiology, 2012. **81**(2): p. 360-365.

11. Takahashi, N., et al., *Dual-Energy CT Iodine-Subtraction Virtual Unenhanced Technique to Detect Urinary Stones in an Iodine-Filled Collecting System: A*

Phantom Study. AJR. American journal of roentgenology, 2008. **190**(5): p. 1169-1173.

12. Zhang, L.-J., et al., *Liver virtual non-enhanced CT with dual-source, dual-energy CT: a preliminary study.* European Radiology, 2010. **20**(9): p. 2257-2264.

13. Sommer, C.M., et al., *Iodine removal in intravenous dual-energy CT-cholangiography: Is virtual non-enhanced imaging effective to replace true non-enhanced imaging?* European Journal of Radiology, 2012. **81**(4): p. 692-699.

14. Ruzsics, B., et al., *Dual-energy CT of the heart for diagnosing coronary artery stenosis and myocardial ischemia-initial experience.* European radiology, 2008. **18**(11): p. 2414-2424.

15. Lu, G.M., et al., *Dual-Energy CT of the Lung.* American Journal of Roentgenology, 2012. **199**(5_supplement): p. S40-S53.

16. Zhang, L.-J., et al., *Dual-energy CT angiography in the evaluation of intracranial aneurysms: image quality, radiation dose, and comparison with 3D rotational digital subtraction angiography.* American Journal of Roentgenology, 2010. **194**(1): p. 23-30.

17. Postma, A.A., et al., *Dual-energy CT of the brain and intracranial vessels.* American Journal of Roentgenology, 2012. **199**(5_supplement): p. S26-S33.

18. Petrongolo, M. and L. Zhu, *Noise Suppression for Dual-Energy CT through Entropy Minimization.* 2015.

19. Niu, T., et al., *Iterative image-domain decomposition for dual-energy CT.* Medical Physics, 2014. **41**(4): p. 041901.

20. Alvarez, R.E., *Dimensionality and noise in energy selective x-ray imaging.* Medical physics, 2013. **40**(11): p. 111909.

21. Johns, P.C. and M.J. Yaffe, *Theoretical optimization of dual-energy x-ray imaging with application to mammography.* Medical Physics, 1985. **12**(3): p. 289-296.

22. Johnson, T.C., et al., *Material differentiation by dual energy CT: initial experience.* European Radiology, 2007. **17**(6): p. 1510-1517.

23. Xia, T., A.M. Alessio, and P.E. Kinahan, *Dual energy CT for attenuation correction with PET/CT.* Medical physics, 2014. **41**(1): p. 012501.

24. Graser, A., et al., *Dual energy CT: preliminary observations and potential clinical applications in the abdomen.* European Radiology, 2009. **19**(1): p. 13-23.

25. Flohr, T.G., et al., *First performance evaluation of a dual-source CT (DSCT) system.* European radiology, 2006. **16**(2): p. 256-268.

26. Engel, K.J., C. Herrmann, and G. Zeitler, *X-ray scattering in single- and dual-source CT.* Medical Physics, 2008. **35**(1): p. 318-332.

27. Karçaaltıncaba, M. and A. Aktaş, *Dual-energy CT revisited with multidetector CT: review of principles and clinical applications.* Diagn Interv Radiol, 2011. **17**(3): p. 181-194.

28. Zou, Y. and M.D. Silver. *Analysis of fast kV-switching in dual energy CT using a pre-reconstruction decomposition technique*. 2008.

29. Kang, M.-J., et al., *Dual-Energy CT: Clinical Applications in Various Pulmonary Diseases.* RadioGraphics, 2010. **30**(3): p. 685-698.

30. Boll, D.T., et al., *Coronary Stent Patency: Dual-Energy Multidetector CT Assessment in a Pilot Study with Anthropomorphic Phantom 1.* Radiology, 2008. **247**(3): p. 687-695.

31. Riederer, S.J. and C.A. Mistretta, *Selective iodine imaging using K-edge energies in computerized x-ray tomography.* Medical Physics, 1977. **4**(6): p. 474-481.

32. Lehmann, L.A., et al., *Generalized image combinations in dual KVP digital radiography.* Medical Physics, 1981. **8**(5): p. 659-667.

33. Emil, Y.S., Z. Yu, and P. Xiaochuan, *Impact of polychromatic x-ray sources on helical, cone-beam computed tomography and dual-energy methods.* Physics in Medicine and Biology, 2004. **49**(11): p. 2293.

34. Maaß, C., M. Baer, and M. Kachelrieß, *Image-based dual energy CT using optimized precorrection functions: A practical new approach of material decomposition in image domain.* Medical Physics, 2009. **36**(8): p. 3818-3829.

35. Sukovic, P. and N.H. Clinthorne, *Penalized weighted least-squares image reconstruction for dual energy X-ray transmission tomography.* Medical Imaging, IEEE Transactions on, 2000. **19**(11): p. 1075-1081.

36. Sidky, E.Y., Y. Zou, and X. Pan, *Impact of polychromatic x-ray sources on helical, cone-beam computed tomography and dual-energy methods.* Physics in medicine and biology, 2004. **49**(11): p. 2293.

37. Maaß, C., E. Meyer, and M. Kachelrieß, *Exact dual energy material decomposition from inconsistent rays (MDIR).* Medical Physics, 2011. **38**(2): p. 691-700.

38. Boedeker, K. and M. McNitt-Gray, *Application of the noise power spectrum in modern diagnostic MDCT: part II. Noise power spectra and signal to noise.* Physics in medicine and biology, 2007. **52**(14): p. 4047.

39. Boedeker, K.L., V.N. Cooper, and M.F. McNitt-Gray, *Application of the noise power spectrum in modern diagnostic MDCT: part I. Measurement of noise power spectra and noise equivalent quanta.* Physics in medicine and biology, 2007. **52**(14): p. 4027.

40. Riederer, S.J., N.J. Pelc, and D.A. Chesler, *The noise power spectrum in computed x-ray tomography.* Physics in medicine and biology, 1978. **23**(3): p. 446.

41. Kijewski, M.F. and P.F. Judy, *The noise power spectrum of CT images.* Physics in medicine and biology, 1987. **32**(5): p. 565.

42. Roessl, E., A. Ziegler, and R. Proksa, *On the influence of noise correlations in measurement data on basis image noise in dual-energylike x-ray imaging.* Medical physics, 2007. **34**(3): p. 959-966.

43. Graser, A., et al., *Dual energy CT: preliminary observations and potential clinical applications in the abdomen.* European radiology, 2009. **19**(1): p. 13-23.

44. Kalender, W.A., E. Klotz, and L. Kostaridou, *An algorithm for noise suppression in dual energy CT material density images.* Medical Imaging, IEEE Transactions on, 1988. **7**(3): p. 218-224.

45. Warp, R.J. and J.T. Dobbins, *Quantitative evaluation of noise reduction strategies in dual-energy imaging.* Medical Physics, 2003. **30**(2): p. 190-198.

46. Cao, Q., et al., *Least squares approach in measurement-dependent filtering for selective medical images.* Medical Imaging, IEEE Transactions on, 1988. **7**(2): p. 154-160.

47. Rutherford, R.A., B.R. Pullan, and I. Isherwood, *Measurement of effective atomic number and electron density using an EMI scanner.* Neuroradiology, 1976. **11**(1): p. 15-21.

48. Hinshaw, D.A. and J.T. Dobbins III. *Recent progress in noise reduction and scatter correction in dual-energy imaging*. in *Medical Imaging 1995*. 1995. International Society for Optics and Photonics.

49. Wang, G. and M. Vannier, *Helical CT image noise—analytical results.* Medical physics, 1993. **20**(6): p. 1635-1640.

50. Macovski, A., et al., *Measurement-dependent filtering: a novel approach to improved SNR.* Medical Imaging, IEEE Transactions on, 1983. **2**(3): p. 122-127.

51. Dong, X., T. Niu, and L. Zhu, *Combined iterative reconstruction and image-domain decomposition for dual energy CT using total-variation regularization.* Medical physics, 2014. **41**(5): p. 051909.

52. Zhu, L., J. Wang, and L. Xing, *Noise suppression in scatter correction for cone-beam CT.* Medical Physics, 2009. **36**(3): p. 741-752.

53. Strutz, T., *Data Fitting and Uncertainty (A practical introduction to weighted least squares and beyond). Vieweg+ Teubner*. 2010, ISBN 978-3-8348-1022-9.

54. Canny, J., *A Computational Approach to Edge Detection.* Pattern Analysis and Machine Intelligence, IEEE Transactions on, 1986. **PAMI-8**(6): p. 679-698.

55. Prewitt, J.M., *Object enhancement and extraction.* Picture processing and Psychopictorics, 1970. **10**(1): p. 15-19.

56. Lee, J.-S., *Digital image smoothing and the sigma filter.* Computer Vision, Graphics, and Image Processing, 1983. **24**(2): p. 255-269.

57. Morel, J.-M., A. Buades, and T. Coll, *Local Smoothing Neighborhood Filters*, in *Handbook of Mathematical Methods in Imaging*. 2011, Springer. p. 1159-1201.

58. Niu, T. and L. Zhu, *Scatter correction for full-fan volumetric CT using a stationary beam blocker in a single full scan.* Medical Physics, 2011. **38**(11): p. 6027-6038.

59. Baek, J. and N.J. Pelc, *The noise power spectrum in CT with direct fan beam reconstruction.* Medical Physics, 2010. **37**(5): p. 2074-2081.

60. Siewerdsen, J., I. Cunningham, and D. Jaffray, *A framework for noise-power spectrum analysis of multidimensional images.* Medical physics, 2002. **29**(11): p. 2655-2671.

61. Joan, H., M. Boyd, and B.G. Peter, *Cone beam computerized tomography: the effect of calibration of the Hounsfield unit number to electron density on dose calculation accuracy for adaptive radiation therapy.* Physics in Medicine and Biology, 2009. **54**(15): p. N329.

62. Petrongolo, M., X. Dong, and L. Zhu, *A general framework of noise suppression in material decomposition for dual-energy CT.* Medical physics, 2015. **42**(8): p. 4848-4862.